

On the genesis and dynamics of Madden–Julian oscillation-like structure formed by equatorial adjustment of localized heating

Masoud Rostami^{1,2}  | Bowen Zhao³ | Stefan Petri¹ 

¹Potsdam Institute for Climate Impact Research (PIK), Member of the Leibniz Association, Potsdam, Germany

²Laboratoire de Météorologie Dynamique (LMD), Sorbonne University (SU), Ecole Normale Supérieure (ENS), CNRS, Paris, France

³Department of Earth and Planetary Sciences, Yale University, New Haven, Connecticut

Correspondence

M. Rostami, Potsdam Institute for Climate Impact Research (PIK), Member of the Leibniz Association, P.O. Box 60 12 03, D-14412 Potsdam, Germany.
Email: rostami@pik-potsdam.de

Funding information

H & M Foundation, Grant/Award Number: 20A048

Abstract

By means of a new multilayer pseudo-spectral moist-convective thermal rotating shallow-water (mcTRSW) model in a full sphere, we present a possible equatorial adjustment beyond Gill's mechanism for the genesis and dynamics of the Madden–Julian oscillation (MJO). According to this theory, an eastward-propagating MJO-like structure can be generated in a self-sustained and self-propelled manner due to nonlinear relaxation (adjustment) of a large-scale positive buoyancy anomaly, depressed anomaly, or a combination of these, as soon as this anomaly reaches a critical threshold in the presence of moist convection at the Equator. This MJO-like episode possesses a convectively coupled “*hybrid structure*” that consists of a “quasi-equatorial modon” with an enhanced vortex pair and a convectively coupled baroclinic Kelvin wave (BKW), with greater phase speed than that of dipolar structure on an intraseasonal time-scale. Interaction of the BKW, after circumnavigating the entire Equator, with a new large-scale buoyancy anomaly may contribute to excitation of a recurrent generation of the next cycle of MJO-like structure. Overall, the generated “*hybrid structure*” captures a few of the crudest features of the MJO, including its quadrupolar structure, convective activity, condensation patterns, vorticity field, phase speed, and westerly and easterly inflows in the lower and upper troposphere. Although moisture-fed convection is a necessary condition for the “*hybrid structure*” to be excited and maintained in the proposed theory in this study, it is fundamentally different from moisture-mode theories, because the barotropic equatorial modon and BKW also exist in “dry” environments, while there are no similar “dry” dynamical basic structures in moisture-mode theories. The proposed theory can therefore be a possible mechanism to explain the genesis and backbone structure of the MJO and to converge some theories that previously seemed divergent.

KEY WORDS

equatorial modon, geostrophic adjustment, Madden–Julian oscillation, moist-convective thermal rotating shallow-water model

1 | INTRODUCTION

More than half of the globe is considered “the Tropics”; thus a proper understanding of the tropical atmosphere is crucial for improving global weather forecasts, as well as for projections of global climate change. Matsuno (1966) and Gill (1980) present the foundations of equatorial waves by utilizing the one-layer version of the shallow-water model on the equatorial β -plane. Let us recall that rotating shallow-water (RSW) models are effective and low-cost numerical tools with which to study the large-scale dynamics of the oceans and atmosphere based on vertically averaged primitive equations between pairs of material surfaces in vertical coordinates. The RSW model in the equatorial β -plane is an archetype model for understanding dynamics in the Tropics. The derived spectrum of equatorial waves is highly consistent with outgoing long-wave radiation (OLR) data (Wheeler and Kiladis, 1999), except for a branch corresponding to slowly eastward-moving motions associated with the Madden–Julian oscillation (MJO). The MJO is the prominent fluctuation in tropical weather over a 30–90 day cycle (Madden and Julian, 1972; 1994). This large-scale circulation of enhanced deep convection moves slowly eastward from the Indian Ocean and then passes over the maritime continent and finally dies out over the Pacific Ocean. The MJO is accompanied by extreme rainfall and wind over an area roughly 1,500 km in latitude and 4,500 km in longitude (Zhang *et al.*, 2020) and has a great impact on both tropical moist-air circulation and midlatitude environment variables on the intraseasonal time-scale (Vitart and Molteni, 2010). There have been several attempts to explain basic features of the MJO in terms of various dynamic mechanisms. A comprehensive description of the existing state of theories of the MJO has been provided in recent reviews by Zhang *et al.* (2020) and Jiang *et al.* (2020). In particular, Kim and Zhang (2021) recently found a slowed-down Kelvin-wave (KW) solution that resembles intraseasonal periodicity on the planetary scale and eastward propagation like that of the MJO by adding momentum damping to the linear equatorial shallow-water equations in a “dry” environment. Theories of the MJO are still diverse and further advancements in understanding the crudest dynamics of the MJO are unavoidable (Zhang *et al.*, 2020). Previous theoretical studies, modeling, and field observations, in terms of linear and nonlinear equatorial waves of the MJO, have contributed positively to our understanding of the MJO; nevertheless, a few dynamical aspects of the MJO are not fully understood. Some of these aspects include initiation of the MJO, its backbone structure, the role of moist convection in determining the phase speed, the evolution of potential temperature in the lower and upper troposphere

during MJO evolution, and the roles of Rossby and Kelvin waves in the MJO’s eastward propagation mechanism.

The present study aims to shed light on these aspects and to show that there are high degrees of convergence between some theories that previously seemed divergent. The theory that is particularly relevant to this research is one that regards the MJO as a “*hybrid structure*”, which consists of a “quasi-equatorial modon” and convectively coupled baroclinic Kelvin wave (CCBKW: Rostami and Zeitlin, 2020a). This theory has been developed in a step-wise manner, with a hierarchy of models with different levels of complexity, in such a way that each step has provided a solid basis for further theoretical studies in the next step. All steps are described below for better understanding.

1. In the first step, it was shown that the barotropic equatorial modon has a persistent eastward propagation for a long time span in a “dry” or adiabatic environment (Yano and Tribbia, 2017; Rostami and Zeitlin, 2019a). A modon is defined as an exact, form-preserving, uniformly translating, horizontally localized, nonlinear solution to the inviscid quasigeostrophic equations. Yano and Tribbia (2017) illustrated a barotropic modon from solutions of Tribbia (1984) and Verkley (1984) on a sphere. Rostami and Zeitlin (2019a) obtained a similar coherent dipolar structure, the so-called equatorial modon, via the process of ageostrophic adjustment from the analytical asymptotic modon solutions of the vorticity equation obtained at the limit of small pressure perturbations in the equatorial β -plane (see the Appendix). Numerical simulation with a high-resolution shallow-water model in the equatorial β -plane that is initialized with analytical asymptotic modon solutions leads to a steady dipolar structure, which propagates eastward coherently. One fundamental difference of our proposed MJO theory encompassing the modon as one of the key components of its proposed structure is that equatorial modons have an exact asymptotic solution and crystal-clear structure; furthermore, eastward propagation and small phase speed are innate characters of them that exist even in “dry” environments. Such a feature does not exist in moisture-mode theories, in which no dry dynamical basic structure exists. The applied dynamical regime in the RSW model by Rostami and Zeitlin (2019a) corresponds to the so-called long-wave approximation in oceanography (Gill, 1982), which arises at the limit of small pressure variations and gives, to leading order, a vorticity equation that does allow for modon solutions. This quasibarotropic regime is the RSW analog of the Charney (1963) nondivergent balance model for the equatorial atmosphere. According to scale analysis by Charney, synoptic-scale tropical adiabatic

motions should obey barotropic vorticity dynamics. The modon solutions in a quasigeostrophic (QG) model with a finite deformation radius on a midlatitude tangent plane were already introduced by Larichev and Reznik (1976) and then Flierl *et al.* (1980) showed the effects of baroclinicity with their two-layer generalized version of the QG model. Nevertheless, the QG approximation loses its full validity in the vicinity of the equatorial β -plane. It is therefore no wonder this approach has been overlooked by the community. In the first step, the main downsides of the equatorial modon's structure compared with the MJO were incompatibility in vertical structure due to the barotropic structure of the equatorial model and lack of a mechanism to explain its genesis. The presence of dipolar structure in the MJO is well established in the literature (e.g. Lau and Phillips, 1986; Matthews, 2000; Zhang and Ling, 2012); indeed, Wang *et al.* (2019) analyzed the vorticity variability associated with the MJO and reported the existence of a dipolar-vortex signal. This analysis supported the existence of a strongly nonlinear modon solution.

2. In the second step, it was demonstrated, for the first time, that the equatorial modon's structure can also emerge from the process of equatorial adjustment of a localized large-scale depression-type disturbance as soon as it reaches a triggering state in the standard moist-convective rotating shallow-water (mcRSW) model on the equatorial β -plane (Rostami and Zeitlin, 2019b). The critical threshold, triggering state, or tipping point in this context refers to a state in which a small additional perturbation transmits the large-scale evolution and structure of the system to an eastward propagation. From this step on, there is a transition from analytical to numerical solutions. Notably, these slowly eastward-propagating modons arise from such equatorial adjustment only in the presence of moist-convective feedback, not in the “dry” case. However, once an equatorial modon is created, it can survive for a long time span even in a “dry” environment. This finding opened a new window to look for the dynamical relation between equatorial adjustment and stimulated eastward-propagating structures. Indeed, this result undermined the universality of the well-known classical Gill (Gill, 1980; 1982) theory of tropical circulation due to localized heating. According to Gill's mechanism, when the imposed heating is symmetric about the Equator, the response can be interpreted as steady, damped Kelvin and Rossby waves extending to the east and west of the heating, respectively. Zhao *et al.* (2021) could produce a similar eastward propagation due to geostrophic adjustment like that of Rostami and Zeitlin (2019b) with a moist-convective RSW model on a sphere.
3. In the third step, further studies showed that increasing baroclinicity eventually leads to loss of coherency and arrest of eastward propagation (Rostami and Zeitlin, 2020b). Following the process of equatorial adjustment, Rostami and Zeitlin (2020a) studied the process of relaxation (adjustment) of localized large-scale pressure anomalies in the lower equatorial troposphere, and showed that such phenomena can engender coherent structures strongly resembling some of the crudest features of MJO events, as seen in vorticity, pressure, phase speed, time span, and condensation patterns. It is worth noting that by using a Lagrangian atmospheric model, Liang *et al.* (2021) re-examined the hypothesis of the generation of MJO structure due to equatorial adjustment of large-scale localized heating (Rostami and Zeitlin, 2020a) by imposing warm sea-surface temperature anomalies of different aspect ratios and magnitudes and could observe robust generation of an MJO event. The aforementioned equatorial adjustment simulation in moist-convective environments by the mcRSW model was accomplished by forcing a negative pressure anomaly, with an invariant gradient of potential temperature.
4. In the present study, we intend to advance the recently proposed theory by Rostami and Zeitlin (2020a) one step further by completing the missing part of their model, which is the variation of potential temperature. In order to overcome this bottleneck, we have implemented a multilayer pseudo-spectral moist-convective thermal rotating shallow-water (mcTRSW) model (see Section 2) to capture evolution of the buoyancy field and its interaction with other fields explicitly in the lower troposphere. All the principal equations of the mcTRSW model and numerical scheme in this study are different from those of the mcRSW model by Rostami and Zeitlin (2020a). Our results show that an MJO-like skeleton can be agitated in a self-sustained and self-propelled manner as a “*hybrid structure*” right after a large-scale localized heating and/or depression-type disturbance in the lower troposphere reaches a triggering state in a moist-convective environment. The “*hybrid structure*” is constituted by a combination of a dipolar structure or quasi-equatorial modon and a CCBKW that lasts for an intraseasonal time-scale. The baroclinic Kelvin wave (BKW) then detaches from the dipole due to its higher eastward phase speed. It is shown that catching up and interaction of the circumnavigated BKW with a new large-scale positive buoyancy anomaly may trigger the recurrent generation of a new MJO-like structure, and its interaction with the residue of the eastward-evolving part from the previous cycle weakens the residue of

the eastward-propagating wave. The latter interaction is accompanied by subsequent destabilization due to shear in vorticity and an elongated temperature front. The proposed mechanism of this theory captures a few basic features of the MJO structure as seen in its eastward propagation with low phase speed, quadrupolar structure, convective activity, condensation patterns, vortex-pair structure, westerly and easterly inflows in the lower and upper troposphere, and episodic recurrent generation on an intraseasonal time-scale in the presence of a large-scale warm pool.

The article is organized as follows. In Section 2 we describe the multilayer pseudo-sparse spectral mcTRSW model with minimal parameterization in the full sphere. Then, in Section 3, by means of the mcTRSW model we examine the adjustment scenarios by applying the model for the equatorial adjustment of large-scale localized positive potential temperature and negative thickness anomalies. We show that both approaches coincide in generating the “*hybrid structure*” with a high order of similarity. Section 4 contains a comprehensive comparison of the results with the MJO. Conclusion and further discussion are in Section 5.

2 | MODEL DESCRIPTION AND SETUP OF NUMERICAL EXPERIMENTS

2.1 | Multilayer thermal rotating shallow-water model

In spite of remarkable theoretical frameworks to affirm the capabilities of the TRSW model, a sporadic number of multilayer numerical implementations of mcTRSW models on a sphere exist among atmospheric models. In the classical setup of shallow-water models, fluid is homogeneous, incompressible, and under hydrostatic balance (cf. Zeitlin, 2018), so gradients of mean temperature and density are invariant in this setup. However, the TRSW models employ inhomogeneous layers, which allow horizontal variations in material properties in the RSW model (Schopf and Cane, 1983; Ripa, 1993). Thus, the TRSW equations are also called the inhomogeneous-layer model in the literature (cf. Ripa, 1996). The concept of TRSW has a profound theoretical background and a relatively long history in the literature. For instance, this approach has been applied to examine dynamical effects of a well-mixed planetary boundary layer (Lavoie, 1972) or to formulate a reduced two-dimensional system governing deep atmospheric motions under simple classes of stratification (Salby, 1989). The TRSW model in some cases has been explained as

a model for an upper active layer of fluid on top of a lower inert layer (Warneford and Dellar, 2013). Ripa (1993) reorganized a framework for a multilayer thermal RSW model and a low-frequency approximation (Ripa, 1996) of the model. Recently, another generalization of Ripa’s single-layer model (Ripa, 1995) to an arbitrary number of layers with stratification and shear has been rederived by Beron-Vera (2021). Using a novel well-balanced central upwind scheme, Kurganov *et al.* (2021b) compared the TRSW model with the isothermal RSW model for dynamical processes of evolution of isolated vortices in the midlatitude β -plane. In another approach, Zerroukat and Allen (2015) presented a TRSW model that is derived from a three-dimensional Boussinesq approximation of the hydrostatic Euler equations, where they used the absolute temperature as the thermodynamic variable.

In the first place, we include variation of potential temperature in the “dry” multilayer TRSW model, in which the density of a fluid can vary. For this purpose, we start with vertical integration of the atmospheric primitive equations in terms of the pseudo-height isobaric vertical coordinates (Hoskins and Bretherton, 1972). We write them down in Cartesian coordinates (x, y, z):

$$\frac{\partial \mathbf{v}_h}{\partial t} + \mathcal{V} \cdot \nabla \mathbf{v}_h + f \hat{\mathbf{z}} \times \mathbf{v}_h = -\nabla_h \Phi, \quad (1a)$$

$$\frac{\partial \Phi}{\partial z} = g \frac{\theta}{\theta_s}, \quad (1b)$$

$$\nabla_h \cdot \mathbf{v}_h + \frac{\partial w}{\partial z} = 0, \quad (1c)$$

$$\frac{\partial \theta}{\partial t} + \mathbf{v}_h \cdot \nabla_h \theta + w \frac{\partial \theta}{\partial z} = 0. \quad (1d)$$

These equations present the horizontal momentum (Equation 1a), the hydrostatic relation (Equation 1b), the incompressibility (Equation 1c), and the conservation of potential temperature (Equation 1d) respectively. Here $\mathcal{V} = (u, v, w)$ stands for the 3D velocity field, $\mathbf{v}_h = (u, v)$ is its horizontal part, Φ is geopotential, ∇ and ∇_h are three- and two-dimensional gradient operators, respectively, θ is the potential temperature of the fluid, with a reference potential temperature θ_s at sea level, and g and $\hat{\mathbf{z}}$ stand for gravity acceleration and the unit vector in the vertical direction, respectively. By considering an m -layer configuration, we proceed with the standard procedure of vertical averaging of Equation 1a between the pseudo-height surfaces $z_i(x, y, t)$ and $z_{i+1}(x, y, t)$ and make the mean-field (columnar motion) approximation, which allows one to split averages of products into products of averages. We will count the layers from bottom to top in this section, that is,

$z_0 < z_1 < \dots < z_m$, $h_i = z_i - z_{i-1}$, where m is the number of layers and z_0 is the lowermost material surface. We thus obtain the following “master” equation:

$$\begin{aligned} (z_i - z_{i-1}) & \left(\frac{\partial \mathbf{v}_i}{\partial t} + (\mathbf{v}_i \cdot \nabla) \mathbf{v}_i + f \hat{\mathbf{z}} \times \mathbf{v}_i \right) \\ & = -\nabla \left(\frac{1}{2} \frac{g \bar{\theta}_i}{\theta_s} (z_i - z_{i-1})^2 + \Phi(z_{i-1}) h_i \right) \\ & + \Phi(z_i) \nabla z_i - \Phi(z_{i-1}) \nabla z_{i-1}. \end{aligned} \quad (2)$$

After averaging, we omitted the subscript “h”. Velocity \mathbf{v} and ∇ will be understood from now on as two-dimensional vectors. We will use the Lagrangian derivative $d_i/dt = \partial/\partial t + \mathbf{v}_i \cdot \nabla$. The layer-averaged buoyancy variable in the atmospheric case is defined as $b_i = \bar{g \theta}_i / \theta_s$, where $\bar{\theta}_i$ is the layer-averaged potential temperature.

From the hydrostatic equation (Equation 1b) we get

$$\begin{aligned} \Phi(z_i) & = \Phi(z_{i-1}) + h_i b_i = \Phi(z_0) \\ & + \sum_{j=1}^i \frac{g \bar{\theta}_j}{\theta_s} h_j = \Phi(z_0) + \sum_{j=1}^i h_j b_j, \end{aligned} \quad (3)$$

where j is the index of the sigma notation. For each layer of the TRSW model, the corresponding vertically integrated equations can be written as

$$\begin{aligned} \frac{d_i \mathbf{v}_i}{dt} + f \hat{\mathbf{z}} \times \mathbf{v}_i & = b_i \nabla z_i + \frac{1}{2} h_i \nabla b_i \\ & - \nabla \left(\Phi(z_0) + \sum_{j=1}^i h_j b_j \right), \end{aligned} \quad (4a)$$

$$\frac{\partial h_i}{\partial t} + \nabla(h_i \mathbf{v}_i) = 0, \quad (4b)$$

$$\frac{d_i b_i}{dt} = 0. \quad (4c)$$

Potential temperature should increase with (pseudo-) height in the atmosphere: namely, the layer with the highest b is at the top, which is upside down relative to the oceanic model. The pseudo-height is a function of pressure: that is, it is a modified pressure coordinate, so it can vary on the ground (the lowermost material surface, z_0) as a free surface while the geopotential $\Phi|_{z_0}$ is constant. A “flat top” boundary condition with constant pressure and, as a consequence, constant z is usually imposed at the uppermost material surface, which can be roughly interpreted as the tropopause. In order to get a two-layer TRSW reduction of the atmospheric primitive equations,

we introduce the thicknesses of the layers: $h_1 = z_1 - z_0$, $h_2 = z_2 - z_1$. The boundary conditions are $\Phi|_{z_0} = \text{constant}$, $\nabla z_2 = 0$. After replacing the pseudo-height surfaces in Equation 4a with thicknesses and taking into account the boundary conditions, the momentum equations in final form, after some simplifications, become

$$\frac{d_1 \mathbf{v}_1}{dt} + f \hat{\mathbf{z}} \times \mathbf{v}_1 = -\frac{1}{2} h_1 \nabla b_1 - b_1 \nabla(h_1 + h_2), \quad (5a)$$

$$\frac{d_2 \mathbf{v}_2}{dt} + f \hat{\mathbf{z}} \times \mathbf{v}_2 = \frac{1}{2} h_2 \nabla b_2 - \nabla(h_1 b_1 + h_2 b_2). \quad (5b)$$

2.2 | Thermo-quasigeostrophic balance relations for the barotropic and baroclinic state

To obtain the thermo-quasigeostrophic (TQG) limit of the “dry” TRSW model in the barotropic case without topography, we utilize the following scaling:

$$\begin{aligned} (u, v) & \sim U, \quad (x, y) \sim L, \quad h \sim H_0(1 + \lambda\eta), \\ b & \sim B(1 + 2\lambda b'), \quad f \sim f_0(1 + \lambda y), \end{aligned} \quad (6)$$

where λ is a small nondimensional parameter and η is a deviation from thickness at rest H_0 . The nondimensional momentum equation, after ignoring the higher-order terms on the right-hand side, is

$$Ro \frac{d\mathbf{v}}{dt} + (1 + \lambda y) \hat{\mathbf{z}} \times \mathbf{v} = -\frac{Bu\lambda}{Ro} \nabla(\eta + b'), \quad (7)$$

where $Bu = BH/f_0^2 L^2$ is the Burger number. With respect to the standard for the quasigeostrophic regime, we assume that deviations of thickness and buoyancy from their mean values are small, e.g. the same order as the Rossby number $Ro = U/f_0 L = \lambda$. If we assume $Bu \approx 1$, then Equation 7 becomes

$$\hat{\mathbf{z}} \times \mathbf{v} = -\nabla(\eta + b') = \nabla\psi, \quad (8)$$

where $\psi = \eta + b'$ is the geostrophic streamfunction.

By similar scaling, we can write down the corresponding nondimensional momentum equations of a two-layer TRSW model that can be deduced from Equation 5. We consider a constant geopotential at the lower boundary. We use the following scaling and represent thicknesses and buoyancy fields as

$$\begin{aligned} (u_{1,2}, v_{1,2}) & \sim U, \quad (x, y) \sim L, \\ h_{1,2} & \sim H_0(\delta_{1,2} + \lambda\eta_{1,2}), \\ b_{1,2} & \sim B_0(B_{1,2} + \lambda b'_{1,2}), \quad f \sim f_0, \end{aligned} \quad (9)$$

where $\delta_{1,2} = H_{1,2}/H_0$ denotes the nondimensional thickness, $\eta_{1,2}$ the deviation of thicknesses from $\delta_{1,2}$, $b'_{1,2}$ the buoyancy perturbations, and indices 1, 2 represent the lower and upper layer respectively. This scaling yields

$$\begin{aligned} Ro \frac{d\mathbf{v}_1}{dt} + \sin(\phi) \hat{\mathbf{z}} \times \mathbf{v}_1 \\ = -\frac{Bu\lambda}{Ro} \left(\frac{\delta_1}{2} \nabla b'_1 + B_1 \nabla(\eta_1 + \eta_2) \right), \end{aligned} \quad (10a)$$

$$\begin{aligned} Ro \frac{d\mathbf{v}_2}{dt} + \sin(\phi) \hat{\mathbf{z}} \times \mathbf{v}_2 \\ = -\frac{Bu\lambda}{Ro} \left(\delta_1 \nabla b'_1 + \frac{\delta_2}{2} \nabla b'_2 + B_1 \nabla \eta_1 + B_2 \nabla \eta_2 \right), \end{aligned} \quad (10b)$$

where ϕ is the latitude, so the thermo-geostrophic balance relations between velocity and gradients of pressure and buoyancy perturbations are

$$\sin(\phi) \hat{\mathbf{z}} \times \mathbf{v}_1 = \frac{\delta_1}{2} \nabla b'_1 + B_1 \nabla(\eta_1 + \eta_2), \quad (11a)$$

$$\sin(\phi) \hat{\mathbf{z}} \times \mathbf{v}_2 = \delta_1 \nabla b'_1 + \frac{\delta_2}{2} \nabla b'_2 + B_1 \nabla \eta_1 + B_2 \nabla \eta_2. \quad (11b)$$

2.3 | The multilayer mcTRSW

Let us recall that phase transitions of water vapor with the related latent heat release have already been included in the so-called mcRSW model (Bouchut *et al.*, 2009; Lambaerts *et al.*, 2011a; 2011b; 2012). Evolution of the vertically averaged bulk of humidity and the corresponding effects of condensation and latent heat release upon the air column are defined in the mcRSW model in a simple albeit consistent way. The mcRSW model follows up the semiinal ideas of Gill (1982). An improved version of the model can include precipitable water, vaporization, and precipitation (Rostami and Zeitlin, 2018). The mcRSW model has already been applied to study the effects of moist convection on dynamics of large-scale Earth and planetary jets and vortices (Lambaerts *et al.*, 2012; Lahaye and Zeitlin, 2016; Rostami and Zeitlin, 2017; 2020c; 2022; Rostami *et al.*, 2017). Recently, Kurganov *et al.* (2020) showed that the one-layer configuration of the mcTRSW model, with a well-balanced central upwind scheme, could capture horizontal gradients of potential temperature and their evolution due to moist convection in a self-consistent way. Other well-balanced schemes have already been applied for thermal shallow-water equations (Chertock *et al.*, 2014; Sánchez-Linares *et al.*, 2016).

Inclusion of moist convection in this study is an extension of the one-layer mcTRSW (Kurganov *et al.*, 2020; 2021a). We start by integrating the Lagrangian conservation of the linearized equivalent potential temperature

(moist enthalpy) in the primitive equation of a pair of pseudo-height material surfaces, z_{i-1} and z_i :

$$\lim_{\epsilon \rightarrow 0} \int_{z_{i-1}+\epsilon}^{z_i-\epsilon} \left[\frac{d}{dt} \left(\theta_i + \frac{\mathcal{L}}{C_p} q_i \right) \right] dz = S_i, \quad (12)$$

where $d/dt(\dots) = \partial_t(\dots) + \mathbf{v} \cdot \nabla(\dots)$ is the three-dimensional (3D) Lagrangian derivative, $\mathbf{v} = (u, v, w)$ stands for the 3D velocity field, θ_i represents potential temperature, q_i represents specific humidity, \mathcal{L} is the specific heat of vaporization, C_p denotes the specific heat at constant pressure, and S_i is an external thermal forcing. By considering vertical velocities of the fluid as $w_i = dz_i/dt + \mathcal{W}_i$, $w_{i-1} = dz_{i-1}/dt + \mathcal{W}_{i-1}$, where \mathcal{W}_i presents the extra vertical velocity across the material surface i due to convective fluxes, and the columnar bulk of humidity as $\lim_{\epsilon \rightarrow 0} \int_{z_{i-1}+\epsilon}^{z_i-\epsilon} (\mathcal{L}/C_p) q_i = \bar{q}_i$, we obtain

$$\Delta(\bar{\theta}_i h_i) + \Delta \bar{q}_i + \left(\frac{\bar{q}_i}{h_i} + \bar{\theta}_i \right) (\mathcal{W}_i - \mathcal{W}_{i-1}) = \bar{S}_i, \quad (13)$$

where $\Delta_i(\dots) = \partial/\partial t(\dots) + \nabla \cdot \mathbf{v}_i(\dots)$, $\lim_{\epsilon \rightarrow 0} \int_{z_{i-1}+\epsilon}^{z_i-\epsilon} S_i = \bar{S}_i$, \mathbf{v}_i is the vertically averaged horizontal velocity in layer i , and $\bar{\theta}_i$ stands for the vertically averaged horizontal potential temperature. Indeed, we ascribe the values of dependent variables $\theta(z_i), \theta(z_{i-1}), q(z_i), q(z_{i-1})$ at the vertical boundaries to their average values inside the layer. We therefore obtain $\lim_{\epsilon \rightarrow 0} [\theta(z_i - \epsilon) = \theta(z_{i-1} + \epsilon)] = \bar{\theta}_i$ and similarly $\lim_{\epsilon \rightarrow 0} [(\mathcal{L}/C_p) q(z_i - \epsilon) = (\mathcal{L}/C_p) q(z_{i-1} + \epsilon)] = \bar{q}_i/h_i$. Boundary values can vary with different configurations. In this study, we are looking for the effect of dominant nonadiabatic processes and buoyancy with minimal parameters of convective processes. Thus we consider just the latent heat release due to condensation and do not include precipitable water and related vaporization in the derivation of a simplified two-layer system with a rigid lid. Note that there is no prognostic distribution of water vapor in the model and that its initial distribution is uniform. Condensation, C_i , leads to heating and consequently enhances the total, vertically integrated, potential temperature in the corresponding layer. The potential temperature is proportional to the specific entropy and hence to the heating, with some proportionality to constants $\gamma, \gamma^* > 0$, which gives

$$\Delta(\bar{\theta}_i h_i) = \gamma C_i + \gamma^* \bar{S}_i, \quad (14)$$

where C_i denotes the latent heat release due to condensation, which in this simplified model occurs just in the lower layer. Therefore, γ as the coefficient of C_i shows the contribution of C_i due to its latent heat release as a source for the bulk (vertically integrated) potential temperature and hence the bulk entropy of the air column. Similarly,

γ^* indicates the contribution of \bar{S}_i to the bulk entropy of the air column. γ and γ^* can vary from layer to layer. Indeed, we apply $\bar{S}_i = R_i$ as a simplified thermal Newtonian cooling, $R_i = -(h_i b_i - H_i B_i)/\tau_r$, where τ_r is relaxation time. Substituting Equation 14 in Equation 13, rescaling $\bar{q}_i = (\mathcal{L}g/C_p \theta_s) \int q dz$ and $\bar{R}_i = (g/\theta_s) R_i$, and dropping the bars from now on results in the following equation for a two-layer system:

$$\Delta h_1 = \frac{1}{b_1 + q_1/h_1} [(1 - \gamma)(-C) + (\gamma^* - 1) S_1], \quad (15)$$

where $C = C_1$ is condensation in the lower layer. From Equations 15 and 14, we obtain the Lagrangian derivative of the buoyancy in the lower layer:

$$\begin{aligned} \frac{d_1 b_1}{dt} &= \partial_t b_1 + \mathbf{v}_1 \cdot \nabla b_1 \\ &= \frac{1}{h_1} \left[\left(\frac{(q_1/h_1)(1 - \gamma)}{b_1 + (q_1/h_1)} - 1 \right) (-C) \right. \\ &\quad \left. + \left(\frac{(q_1/h_1)(\gamma^* - 1)}{b_1 + (q_1/h_1)} + 1 \right) S_1 \right]. \end{aligned} \quad (16)$$

Consequently, for the upper layer, by considering $\Delta q_2 = C$ and $\Delta(b_2 h_2) = \gamma^* S_2$, we obtain

$$\Delta h_2 = \frac{-1}{b_2 + q_2/h_2} [(-C) + (1 - \gamma^*) S_2], \quad (17)$$

$$\begin{aligned} \frac{d_2 b_2}{dt} &= \partial_t b_2 + \mathbf{v}_2 \cdot \nabla b_2 \\ &= \frac{1}{h_2} \left[\left(1 - \frac{q_2}{h_2} \right) (-C) + \left(\frac{(q_2/h_2)(\gamma^* - 1)}{b_2 + (q_2/h_2)} + 1 \right) S_2 \right]. \end{aligned} \quad (18)$$

The magnitude of q_i/h_i with respect to other terms like b_i is not negligible, so to capture the precise effect of water vapor it has been kept in the model. One interesting feature of Equations 15 and 16 is that, if $\gamma^* = 1$, then S_1 will disappear on the right-hand side of the h_1 equation and appear just on the right-hand side of the buoyancy equation like the traditional form. Figure 1 represents the sensitivity of the model to γ^* with respect to the energy density of each layer, which is defined as

$$E_i = \int \frac{1}{2} (h_i \mathbf{v}_i^2 + b_i h_i^2) dx dy. \quad (19)$$

Greater values of γ^* yield less loss (gain) of energy density in the lower (upper) layer.

The convective component of vertical velocity produces Stokes drag, which is included in the model (Equation 20a) similarly to Lambaerts *et al.* (2011b). One interesting aspect of the mcTRSW model is that any external heating (S_i) affects both potential temperature and layer thickness, as in atmosphere thermodynamics. For instance, by applying Newtonian cooling, we see this two-way effect in the following Equations 20. In comparison, the heating effect in typical parameterization in modeling the Earth or Mars atmosphere (Rong and Waugh, 2004; Warneford and Dellar, 2013; Seviour *et al.*, 2017; Rostami *et al.*, 2018) appears either in the equations of conservation of potential temperature or in the incompressibility equation, but not both of them. Therefore, all-inclusive, the two layer mcTRSW model reduction of the atmospheric primitive equations with minimal adjustable parameters, assuming $b_i \gg q_i/h_i$, if any, and inclusion of bottom topography (h_b), can be

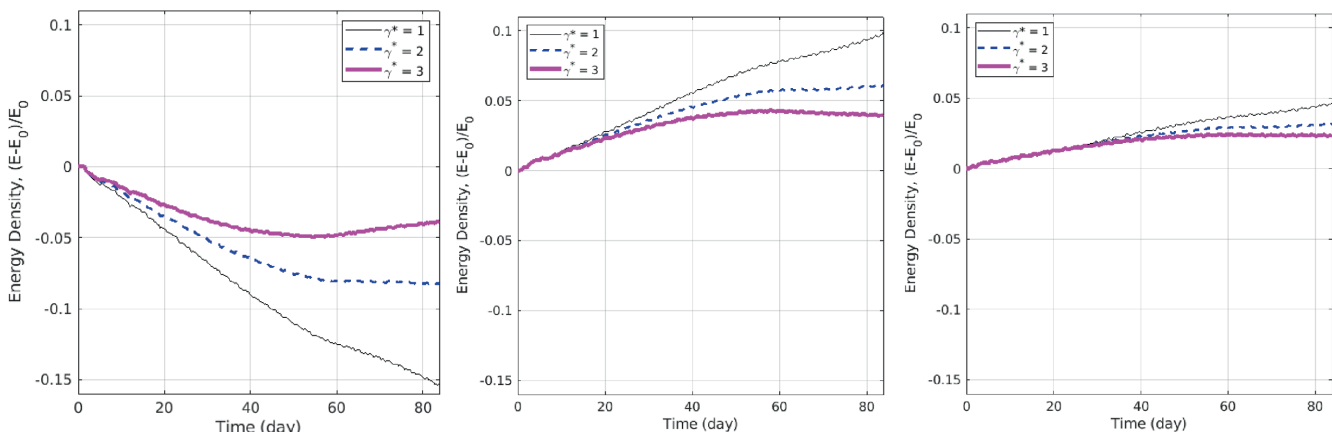


FIGURE 1 Evolution of the thermal shallow-water energy density, as seen in its deviation from the initial value, in the lower layer (left panel), upper layer (middle panel), and overall (right panel) during equatorial adjustment due to an initial positive buoyancy anomaly. E_0 is the initial value of the energy density [Colour figure can be viewed at wileyonlinelibrary.com]

defined by the following set of equations:

$$\frac{d_1 \mathbf{v}_1}{dt} + f \hat{\mathbf{z}} \times \mathbf{v}_1 = -\frac{1}{2} h_1 \nabla b_1 - b_1 \nabla (h_b + h_1 + h_2), \quad (20a)$$

$$\begin{aligned} \frac{d_2 \mathbf{v}_2}{dt} + f \hat{\mathbf{z}} \times \mathbf{v}_2 &= -\frac{1}{2} h_2 \nabla b_2 - \nabla (h_1 b_1) - b_2 \nabla (h_b + h_2) \\ &\quad - \frac{1-\gamma}{b_2 h_2} (\mathbf{v}_2 - \mathbf{v}_1) (C), \end{aligned} \quad (20b)$$

$$\partial_t h_1 + \nabla \cdot (h_1 \mathbf{v}_1) = \frac{1-\gamma}{b_1} (-C) + (1-\gamma^*) \frac{h_1 - (B_1/b_1) H_1}{\tau_r}, \quad (20c)$$

$$\partial_t h_2 + \nabla \cdot (h_2 \mathbf{v}_2) = \frac{1}{b_2} (+C) + (1-\gamma^*) \frac{h_2 - (B_2/b_2) H_2}{\tau_r}, \quad (20d)$$

$$\partial_t b_1 + \mathbf{v}_1 \cdot \nabla b_1 = \frac{1}{h_1} (+C) - \frac{b_1 - (H_1/h_1) B_1}{\tau_r}, \quad (20e)$$

$$\partial_t b_2 + \mathbf{v}_2 \cdot \nabla b_2 = \frac{1}{h_2} (-C) - \frac{b_2 - (H_2/h_2) B_2}{\tau_r}, \quad (20f)$$

$$\partial_t q_1 + \nabla \cdot (q_1 \mathbf{v}_1) = E_s - C, \quad (20g)$$

$$\partial_t q_2 + \nabla \cdot (q_2 \mathbf{v}_2) = C. \quad (20h)$$

The relaxational parameterization of condensation, C , with a relaxation time, τ , is

$$C = \frac{q_1 - Q^s}{\tau} \mathcal{H}(q_1 - Q^s), \quad (21)$$

where \mathcal{H} denotes the Heaviside (step) function and E_s the bulk formula for surface evaporation:

$$E_s = \alpha \frac{|\mathbf{v}_1|}{|\mathbf{v}_{\max}|} (Q^s - q_1) \mathcal{H}(Q^s - q_1), \quad (22)$$

where $|\mathbf{v}_{\max}|$ denotes the maximum amplitude of the lower-layer velocity field, Q^s is the saturation threshold of bulk humidity, and α is an adjustable coefficient. In the simplified version, the saturation value Q^s is taken to be constant, but it can depend on potential temperature according to the Clausius–Clapeyron law (cf. Yano *et al.*, 1995). Parametrization of the condensation (Equation 21) is of the Betts–Miller type (Betts and Miller, 1986), and the parametrization of evaporation (Equation 22) is standard in modeling ocean–atmosphere exchanges (Katsaros, 2001), except for renormalization by the maximum velocity, which is included for convenience. To respect the minimal parametrization approach, we have included just radiative relaxation and surface evaporation

(Equation 22) as the only influences of the boundary layer in the model. An explicit minimal Newtonian viscosity was added to the equations of momentum and buoyancy of the model to inhibit the development of small-scale convective numerical instabilities. Derivation of the spectrum of linear waves in the mcRSW model in the long-wave approximation is discussed in Rostami and Zeitlin (2020a).

It is worth mentioning that a wind-induced surface heat exchange (WISHE) moisture mode in a simplified analytical model produces eastward-propagating modes, with the growth rate greatest at the largest wavelengths (Fuchs and Raymond, 2005; 2017; Fuchs-Stone, 2020). In the convective parameterization of WISHE, variation of moist entropy over time is directly linked to zonal velocity via the WISHE parameter, which is positive for imposed mean westerlies and negative for mean easterlies (Fuchs-Stone and Emanuel, 2022). Therefore, perturbations in surface wind speed enhance the surface enthalpy flux, which consequently increase the moist convective mass flux and temperature.

2.4 | Pseudo-spectral numerical method and setup

Numerical methods for the experiments are devised according to the Dedalus algorithm, which employs spin-weighted spherical harmonics (Lecoanet *et al.*, 2019; Vasil *et al.*, 2019). Gelfand and Shapiro (1956) introduced spin-weighted spherical harmonics for the first time in their Lorenz group studies. One advantage of spin-weighted spherical harmonics is that a combination of spin-weighted spherical harmonics and spinor basis vectors renders differentiation on the sphere similar to a Fourier series; that is, diagonal wavenumber multiplication that remains regular everywhere. We can therefore dump traditional singular gradients at the poles. Spectral discretizations are specified by the Fourier spectral basis for each spatial dimension. It is worth mentioning that some other methods have also been proposed to overcome problems with coordinate singularities in spheres and discs (Boyd and Yu, 2011). The schematic picture of a spin-weighted spherical harmonic transform for a set of shallow-water equations is

$$\partial_t \mathbf{u} + g \nabla h + 2\Omega \mathbf{e}_z \times \mathbf{u} = \mathbf{F} - \mathbf{u} \cdot \nabla \mathbf{u}, \quad (23a)$$

$$\partial_t h + H \nabla \cdot \mathbf{u} = \mathbf{F}(h) - \nabla \cdot (h \mathbf{u}), \quad (23b)$$

where \mathbf{u} is a 2D velocity field in spherical coordinates, $\mathbf{u} = u_\phi \mathbf{e}_\phi + u_\theta \mathbf{e}_\theta$, where $\mathbf{e}_\theta, \mathbf{e}_\phi$ are orthonormal coordinate unit vectors on the surface of the sphere, and $0 \leq \theta \leq \pi$ and $0 \leq \phi \leq 2\pi$ represent polar and circular

angles respectively. Velocity fields and unit vectors on a spin-weighted basis are

$$u_{\pm} = \frac{1}{\sqrt{2}}(u_{\theta} \pm iu_{\phi}), \quad \mathbf{e}_{\pm} = \frac{1}{\sqrt{2}}(\mathbf{e}_{\theta} \mp i\mathbf{e}_{\phi}). \quad (24)$$

We therefore obtain the transformed equations of Equation 23 as

$$\partial_t u_+ + g\nabla_+ h + i2\Omega \cos(\theta) u_+ = F_+ - [\mathbf{u} \cdot \nabla \mathbf{u}]_+, \quad (25a)$$

$$\partial_t u_- + g\nabla_- h - i2\Omega \cos(\theta) u_- = F_- - [\mathbf{u} \cdot \nabla \mathbf{u}]_-, \quad (25b)$$

$$\partial_t h + H(\nabla_+ u_- + \nabla_- u_+) = F(h) - \nabla_+ (h\mathbf{u})_- - \nabla_- (h\mathbf{u})_+, \quad (25c)$$

where $\nabla_{\pm} = (1/\sqrt{2})(\nabla_{\theta} \pm i\nabla_{\phi})$. For a full description of the calculus for vector and tensor operations on the unit 2-sphere with spin-weighted spherical harmonics and its comparison with traditional spherical harmonics, see Vasil *et al.* (2019). By specifying a dealiasing scale factor of 3/2, we set a 384 by 768 global grid along the latitudinal and longitudinal directions, respectively. The two-layer mcTRSW is calibrated with barotropic equatorial Rossby deformation radius $L_d = (\sqrt{gH}/\beta)^{1/2}$, where $H = H_1 + H_2$ is the total nonperturbed layer depth, $H_1 = (1/3)H$, $H_2 = (2/3)H$ in this study, and β denotes the gradient of the Coriolis force in the meridional direction. The zonal and meridional velocity, time, and Earth radius scales are as follows:

$$L \sim L_d, \quad (u, v) \sim \beta L_d^2, \quad t \sim \frac{1}{\beta L_d}, \quad a \sim L_d. \quad (26)$$

The adjustment experiments were initialized with a negative thickness anomaly or positive buoyancy anomaly in the lower layer with $a/L_d = 1.5$. Other ratios of

$a/L_d = [1.0, 1.50, 1.72, 1.88]$ have been tested as well to examine the robustness of the results. The initial nondimensional thickness anomaly is, according to a simplified α -Gaussian equation,

$$h' = h - H = \hat{h} \sqrt{2e} \frac{2^{1/\sigma}}{\sigma} \Gamma\left(\frac{1}{\sigma} + \frac{1}{2}\right) G\left(\frac{r^{\sigma}}{2}, \frac{1}{\sigma} + \frac{1}{2}\right), \quad (27)$$

where r is the spherical distance $r = D(\text{Lat}_0, \text{Lon}_0, \text{Lat}, \text{Lon}) = D(0, 0, \lambda/r_{\text{as}}, \Phi)/L_h$, r_{as} determines the aspect ratio and L_h affects the spatial perturbation sizes. We set $L_h = 0.25$, $r_{\text{as}} = 1.8$, $\sigma = 4$. The method of calculating r is based on great-circle distance with respect to the reference point according to the Haversine formula. $\Gamma(x)$ denotes the Gamma function, $G(r, a) = [1/\Gamma(a)] \int_r^a e^{-t} t^{a-1} dt$, while \hat{h} and σ determine the amplitude and the steepness of the thickness anomaly, respectively. We set the maximum amplitude of the perturbation as $-0.07H$ for experiments that were initialized with a negative thickness anomaly in the lower layer and a similar disturbance with positive sign for the buoyancy anomaly. Water vapor is initialized uniformly and close to the saturation value, Q^s , in the lower layer, $Q_0 = 0.99Q^s$, and far from the saturation value in the upper layer. We set $\gamma = 0.15$ and $\gamma^* = 2$ for the experiments.

The model produces converged solutions to higher precision by applying higher resolution. Propagation of eastward fronts of buoyancy and condensation fields due to events of a large enough buoyancy anomaly in the lower layer, (b_1), shows how the model overcomes (sub)mesoscale instabilities due to thermal effects in the presence of nonlinearity of moist convection (Figure 2) and captures such extreme events. While the package of buoyancy anomaly pursues the condensed air zone, the frontal gradient of the buoyancy anomaly increases with enhanced convection until it reaches a ceased state of eastward propagation and damped condensation. We tested

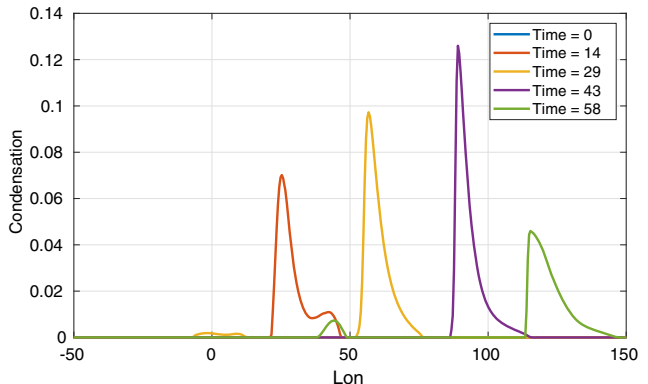
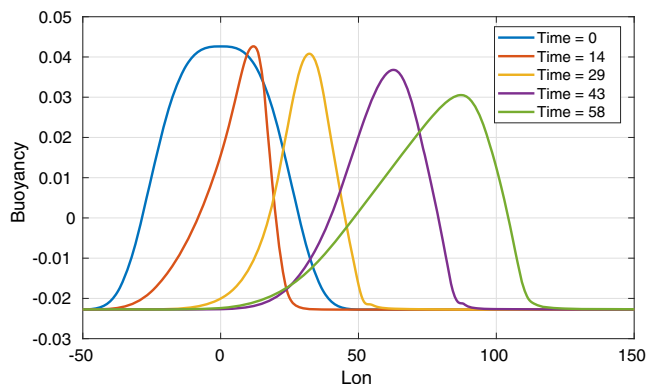


FIGURE 2 Snapshots of buoyancy and condensation in the lower layer at 0.2° latitude during equatorial adjustment of an initial positive buoyancy anomaly at time = 0, 14, 29, 43, 58 [day], consecutively from left to right ($\gamma^* = 1$) [Colour figure can be viewed at wileyonlinelibrary.com]

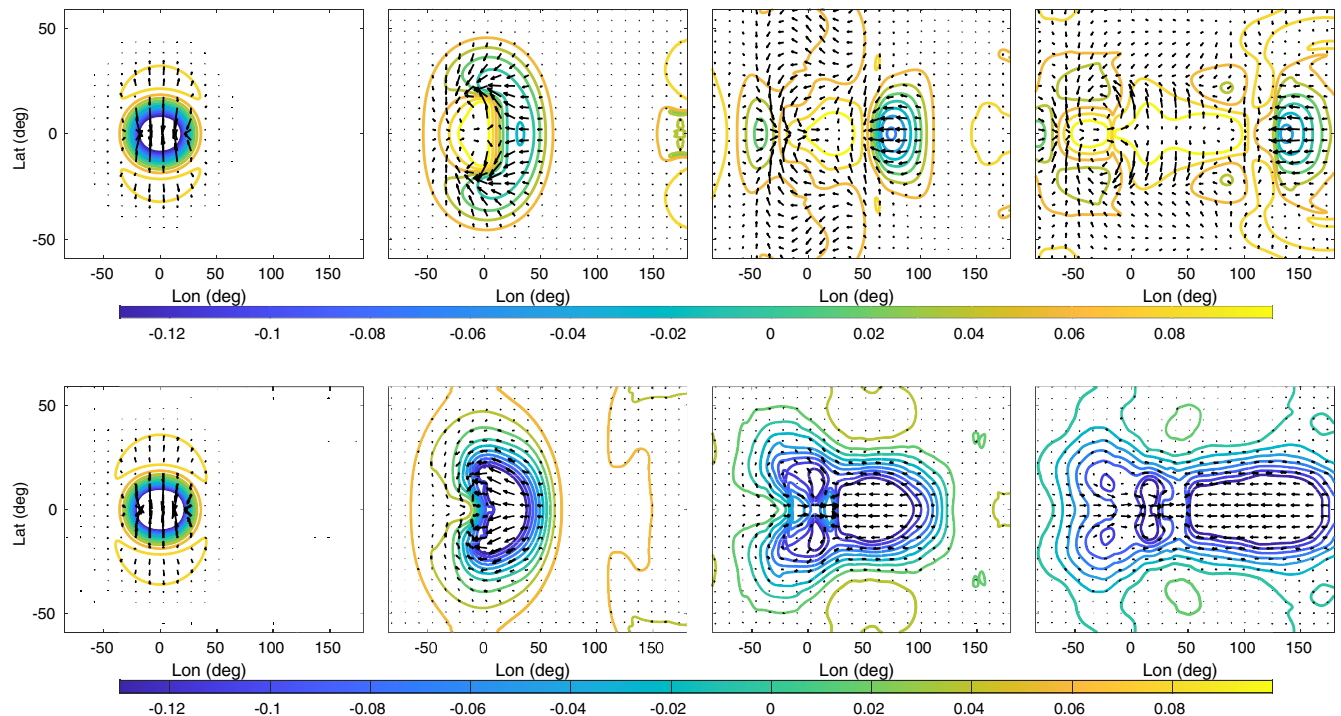


FIGURE 3 Contour levels of baroclinic thickness anomaly (colors) and corresponding spherical velocity field (arrows) at initial stages of equatorial adjustment due to an initial negative thickness anomaly in “dry” (upper row) and moist-convective (lower row) environments. Time = 1, 4, 13, 24 [day], consecutively from left to right [Colour figure can be viewed at wileyonlinelibrary.com]

the model for the benchmark problem of Gill’s mechanism due to a depressed thickness anomaly, as presented in the upper panel of Figure 3. The results are fully consistent with those of the RSW model with finite-volume scheme (cf. Rostami and Zeitlin, 2020b).

3 | RESULTS OF EQUATORIAL ADJUSTMENT

3.1 | Equatorial adjustment beyond Gill’s heat-induced tropical circulation

Recently, it has been found that the well-known Gill theory of tropical circulation due to localized heating is not universal (Rostami and Zeitlin, 2019b). According to Gill’s theory, large-scale localized heating on the equatorial β -plane leads to the generation of westward-moving Rossby and eastward-moving KWs, while Rostami and Zeitlin (2019b) illustrate two other scenarios exist that are missed in Gill’s theory. Both scenarios occur right after the pressure anomaly or potential temperature anomaly reaches a tipping point in the presence of efficient nonadiabatic processes like moist convection. These scenarios are (i) vortices traveling respectively northwest in the Northern and southwest in the Southern hemispheres, (ii) eastward-moving coherent dipolar structures of the

type of equatorial modons, which do not appear in the “dry” adjustment. This experiment was repeated in a full sphere by Zhao *et al.* (2021) and they confirmed the original finding. The same adjustment scenario with baroclinic structure led to generation of an MJO-like structure (Rostami and Zeitlin, 2020a). What was missed in all the aforementioned studies was the role of gradients of potential temperature over the tropical zone. Thus, the two categories of equatorial adjustment that are presented in this study encompass simulations of the evolution of buoyancy over the equatorial zone. These experiments are (1) equatorial adjustment due to a large-scale localized negative thickness anomaly, and (2) equatorial adjustment due to a large-scale localized positive buoyancy anomaly in the lower troposphere. Results show that both approaches produce almost similar results for large-scale eastward propagation that resembles the MJO-like structure.

3.1.1 | Early stages of the adjustment

Figure 3 presents the adjustment of a symmetric negative thickness anomaly that somehow represents a pressure anomaly in “dry” and moist-convective environments. Asymmetric perturbation would yield the emergence of Yanai waves owing to the response of the system to the initial depression. At the onset of thermo-geostrophic

adjustment, a quasi-isotropic inflow moves toward the equatorial center of the anomaly. For a large-scale anomaly, we also observe wind intrusion from the extra-tropical regions. Emission of a packet of fast and short inertia-gravity waves occurs in the initial stages. Then the Coriolis force causes a cyclonic circulation of the velocity on both sides of the equatorial belt. In the presence of moist convection, these cyclones become pronounced and are converted into a quasi-equatorial modon. If the moist convection is weak, then these cyclones will propagate westward as Rossby waves. The other key difference between a “dry” and moist-convective environment is that detachment of long-wave BKW happens much sooner in a “dry” case. The response to adjustment in the “dry” case is similar to Gill’s mechanism (Gill, 1980); that is, Rossby-wave emission in the western sector and KW emission in the eastern sector of the localized anomaly. However, Figure 3 also indicates that a tipping point exists, where an eastward-propagating dipolar structure stems out in the presence of moist-convective diabatic processes as soon as the pressure anomaly reaches this threshold level ($\Delta H_1/H \approx 0.07$). For the case of a similar eastward-propagating equatorial modon in a barotropic structure, we need a greater pressure anomaly as the threshold value (Rostami and Zeitlin, 2019b). Let us recall that latent heat release leads to the intensification of a self-sustained negative pressure anomaly. The main transition from Rossby wave to dipolar or quasi-equatorial modon occurs in the initial stages of adjustment. In baroclinic configurations, this transition occurs under a lower amplitude of pressure anomaly in comparison with barotropic structures (Rostami and Zeitlin, 2019a). Nevertheless, fusion of the dipole with CCBKW and creation of a quadrupole structure (Figure 4a,b) are purely a baroclinic effect. The condensation slows down CCBKW, and at the same time enhances the dipolar gyres in such a way that it can propagate eastward like an equatorial modon. The phase velocity of the CCBKW still has superiority over that of the vortex pair. Once the dipolar structure is generated, it can continue its eastward propagation even in a “dry” environment, although dissipation and baroclinicity can slow down this propagation.

As known, a negative pressure anomaly can generally be translated to a positive potential temperature anomaly, which is denoted as b_1 in the mcTRSW equations. We impose a similar large-scale localized disturbance with positive sign for buoyancy in the lower layer. Most aforementioned mechanisms can also be observed in the adjustment of potential temperature anomaly (Figure 5). Genesis of “*hybrid structure*” is associated with eastward advection of the buoyancy anomaly that is accompanied by the dipolar gyre circulation in a moist-convective environment. Figure 5 presents the evolution of this buoyancy

anomaly, which is a function of potential temperature, and the corresponding vorticity and condensation fields. Dipolar warm cores, which are surrounded by westerly and easterly winds, are prominent sources of the anomalous ascending motions that promote deeper convection. The emerging structure is similar to an equatorial modon. Such a similarity is evident in Figure A1, which presents the streamlines and velocity field of an asymptotic modon in stationary and comoving frames. Warm-front condensation travels ahead of the eastward-propagating buoyancy anomaly (Figure 2). Formation of a “*hybrid structure*” can be seen in the initial stages of vorticity evolution (Figure 4a–c). Moist convection evidently plays a pivotal role at the center of this fusion in order to couple the dipole and the CCBKW (Figure 4c). Enhancement of the moist convection, which can be achieved by lower values of γ , yields stronger attachment of the dipolar structure and the CCBKW; otherwise there will be a weak westerly inflow in the gap between these two structures. Moist convection intensifies these vorticity anomalies. Although at the onset of equatorial adjustment signs of vorticities are similar, soon a weaker vortex pair with opposite signs arises in the upper troposphere and the whole system propagates slowly eastward. A weaker oppositely signed vorticity zone builds up on the eastern edge of the dipole due to the anticyclonic velocity field of the CCBKW. The quadrupole is therefore zonally asymmetric. The two layers have opposite signs of vorticity, particularly outside the hybrid’s center in the eastern sector. In the western sector of the hybrid’s center, a “quasi-barotropic” dipolar structure is dominant.

The intensity of condensation enhances abruptly at the very beginning of the equatorial adjustment (Figure 6), when condensation reaches its peak in the convergent zone. Then the spatial span of condensation shrinks with time while its intensity remains about the same (Figure 4c). The extreme condensation is accompanied by emission of inertia-gravity waves (IGW), which is presented by wave activity in Figure 6. This stimulated state, which is accompanied by dipole genesis, is not repeated during the whole evolution of excited structures. A similar external forcing like intense large-scale localized heating over the warm pool in the lower troposphere, which is able to produce a similar velocity field, in principle, can create similar evolution. However, the existence of such a force in the atmosphere seems rare. Our key finding is that baroclinic adjustment in the lower troposphere in the presence of strong enough moist convection can create such a forcing in a self-sustained and self-propelled manner. The emerged dipolar structure (Figure 9), as a hybrid dipole–CCBKW, has a similar backbone structure to that of the adjusted modon (Rostami and Zeitlin, 2019a).

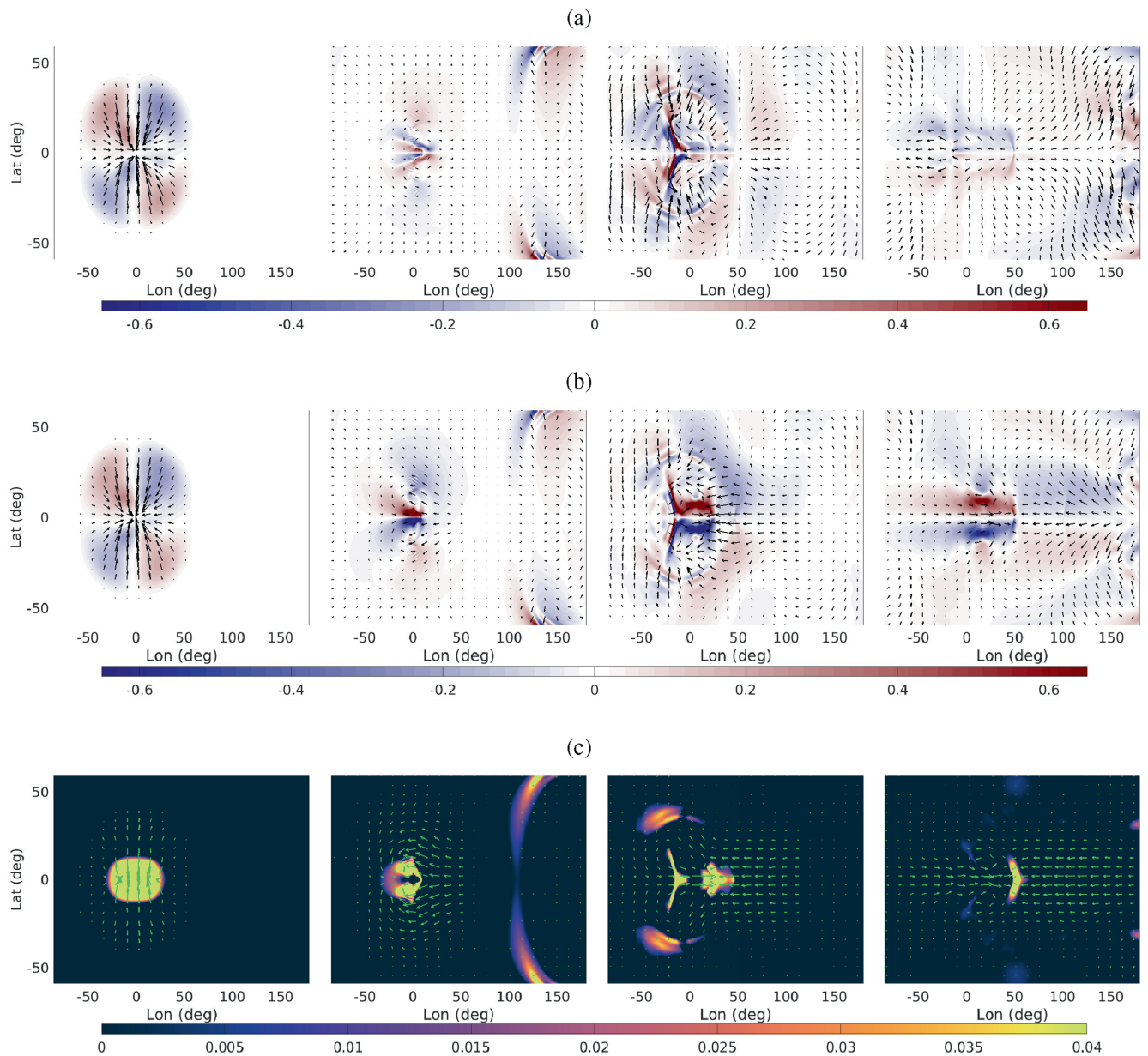


FIGURE 4 Field of vorticity anomaly (colors) in the upper (a) and lower (b) layers and corresponding velocity field (arrows) at the initial stages of equatorial adjustment due to an initial negative thickness anomaly in the lower layer in a moist-convective environment. (c) Corresponding evolution of condensation (color) and baroclinic velocity field (arrows) in the lower layer. Time = 1, 4, 13, 24 [day], consecutively from left to right [Colour figure can be viewed at wileyonlinelibrary.com]

3.1.2 | Late stages of the adjustment

Initial and late stages of adjustment exhibit an eastward propagation (Figures 7–9). Eastward propagation of the buoyancy field, b_1 , also exists in a one-layer barotropic configuration, as seen by Kurganova *et al.* (2020). The buoyancy field acquires an off-equatorial advection at late stages. After the initial stages of the adjustment, we observe an expansion of the CCBKW (Figures 7 and 8), which demonstrates the main source of easterlies in the lower layer. Eventual detachment of the CCBKW leads to weakening

of eastward-propagating westerlies at late stages (Figures 7 and 8). Indeed, from Hovmöller diagrams we can infer that detachment of the CCBKW was never complete, with a significant easterly flow remaining in the frontal sector of the dipolar westerlies, producing a highly convergent zone. It has already been proven theoretically and numerically that baroclinic modon solutions, as a “coherent” structure, do not exist in the 2RSW model (Rostami and Zeitlin, 2020b). The equatorial modon in this context can therefore be regarded as quasibarotropic, with a tendency for barotropization. This feature is compatible with

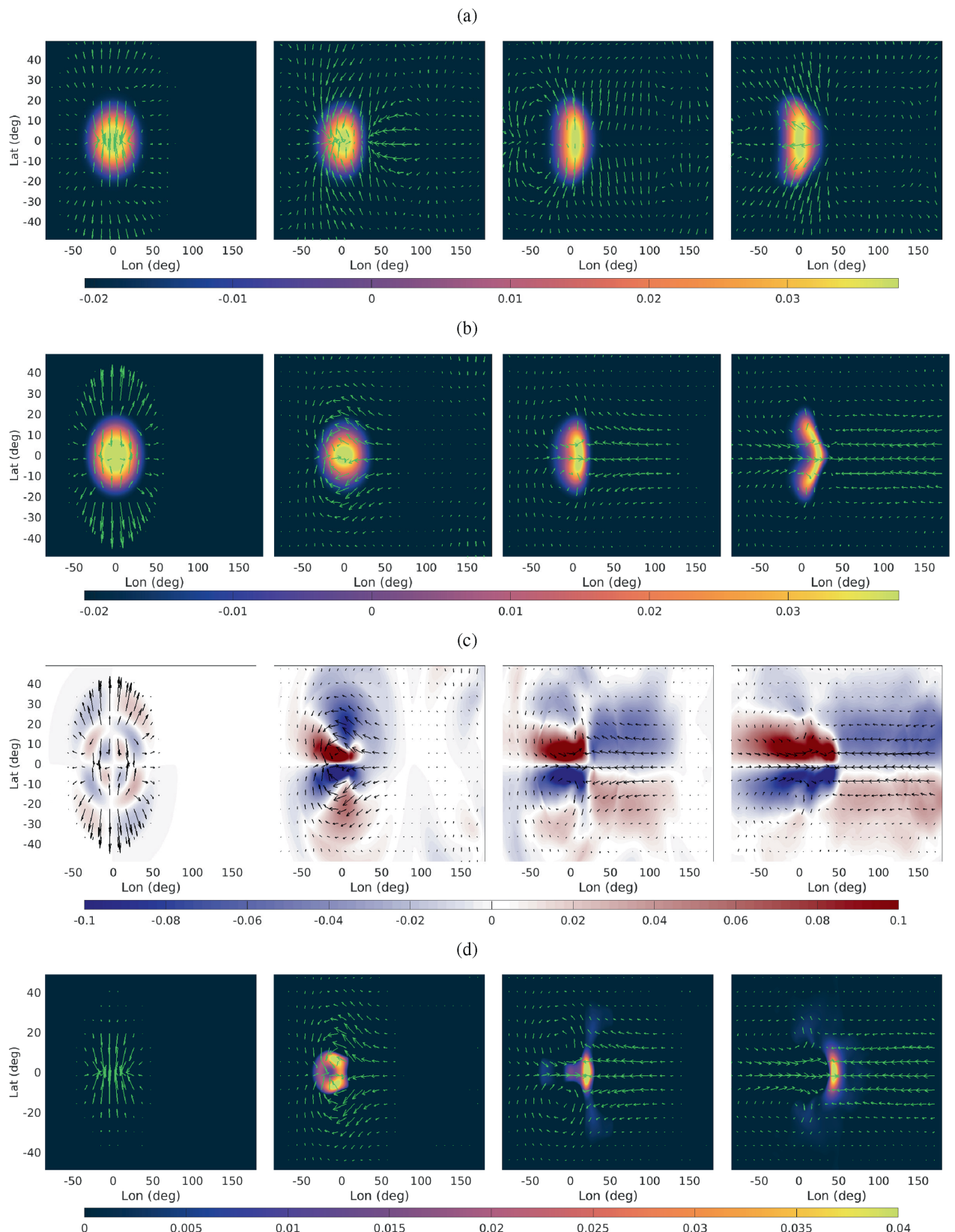


FIGURE 5 Evolution of different fields at the initial stages of equatorial adjustment due to an initial positive buoyancy anomaly in the lower layer in (a) “dry” and (b, c, d) moist-convective environments. Evolution of buoyancy (colors) and corresponding velocity field (arrows) in the lower layer in (a) “dry” and (b) moist-convective environments. (c) Corresponding snapshots of vorticity (colors) and velocity field (arrows). (d) Corresponding snapshots of condensation (colors) and baroclinic velocity field (arrows). Time = 1, 4, 13, 24 [day], consecutively from left to right [Colour figure can be viewed at wileyonlinelibrary.com]

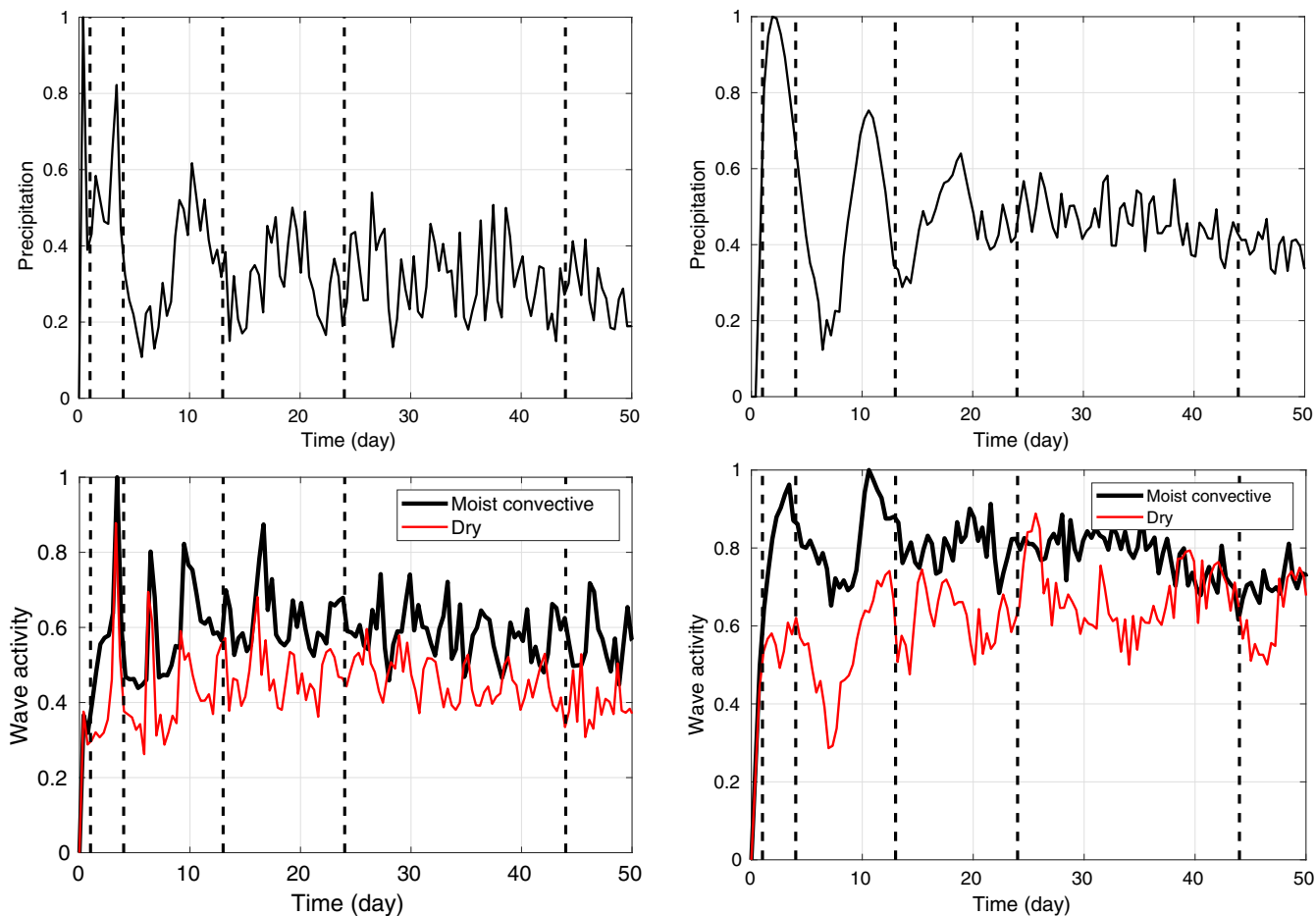


FIGURE 6 Evolution of total condensation (upper row) in the lower layer, between latitudes $[-20^{\circ}, 20^{\circ}]$, normalized by its maximum value, during equatorial adjustment due to an initial negative thickness anomaly (left panels) and positive buoyancy anomaly (right panels). Corresponding normalized wave activities of each experiment in “dry” and moist-convective environments are shown in the lower row. Vertical dashed lines correspond to time = 1, 4, 13, 24, 44 [day] [Colour figure can be viewed at wileyonlinelibrary.com]

the MJO that eventually ceases its eastward propagation. Both barotropic KWs and CCBKWs are interacting with the main dipolar structure in such a way that the former has about 10 interactions while the latter has at least one (Figures 7 and 8). Our results indicate that these interactions lead to loss of coherency and consequently deceleration of eastward propagation. The other factor that causes deceleration of eastward propagation is thermal relaxation, which is introduced as Newtonian cooling in the model. Parameter γ^* controls the strength of this forcing in such a way that greater (smaller) values of γ^* decelerate (ameliorate; see Figure 1) the eastward propagation.

During the elongation of the CCBKW, a secondary eastward-propagating dipole emerges from its western sector (Figures 7 and 9). The first dipolar structure that lags behind eventually turns into westward Rossby waves. We observed a similar phenomenon in another experiment initialized with a positive buoyancy anomaly (Figure 9). While the whole hybrid system is moving eastward, a Rossby-wave tail has a tendency to move westward, which

can cause eventual condensation, westward heat transfer, and interaction with circumnavigating BKWs (Figures 8 and 9). The center of the “*hybrid structure*”, as the most convergent zone, exhibits the most condensation. An east–west asymmetry exists not only in condensation patterns but also in buoyancy evolution (Figure 9).

One other remarkable finding of this study is that interaction of the circumnavigated BKW with the remaining eastward-propagating front at late stages leads to large-scale wave-breaking of the eastward-propagating front, as seen in the vorticity field (Figure 9) or Hovmöller diagrams (Figure 8). Full collision of this wave triggers westward-propagating Rossby waves in both main experiments (Figures 7 and 8).

In the present article, we address the question of recurrent generation of MJO-like structures. When BKW, after circumnavigating all around the Equator, interacts with a new large-scale positive buoyancy anomaly, b_1 , then this interaction triggers recurrent generation, with a new eastward-propagating “*hybrid structure*” (Figure 10). The

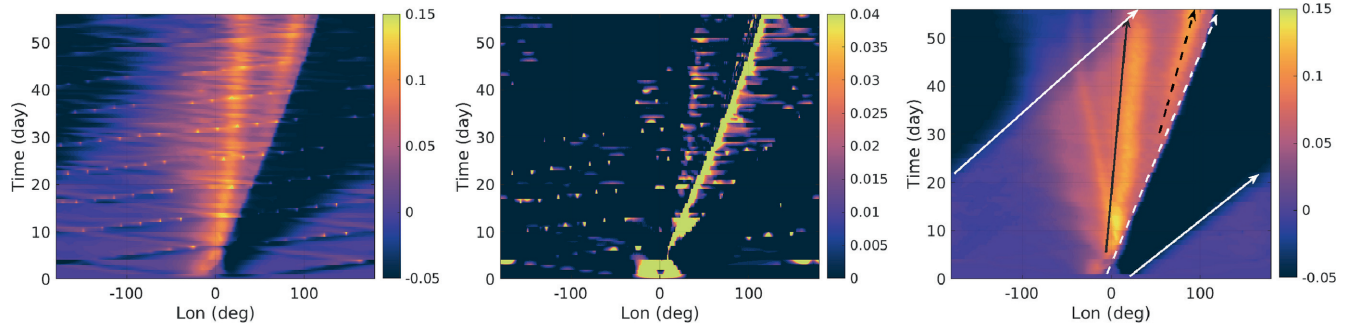


FIGURE 7 Hovmöller diagram of the zonal velocity (left panel), condensation (middle panel), and the baroclinic zonal velocity (right panel) at 0.2° latitude related to equatorial adjustment due to an initial negative thickness anomaly. Solid and dashed arrows indicate the eastern and western fronts of BKW respectively. Two solid and dashed black arrows represent the first and second eastward-propagating dipolar structures [Colour figure can be viewed at wileyonlinelibrary.com]

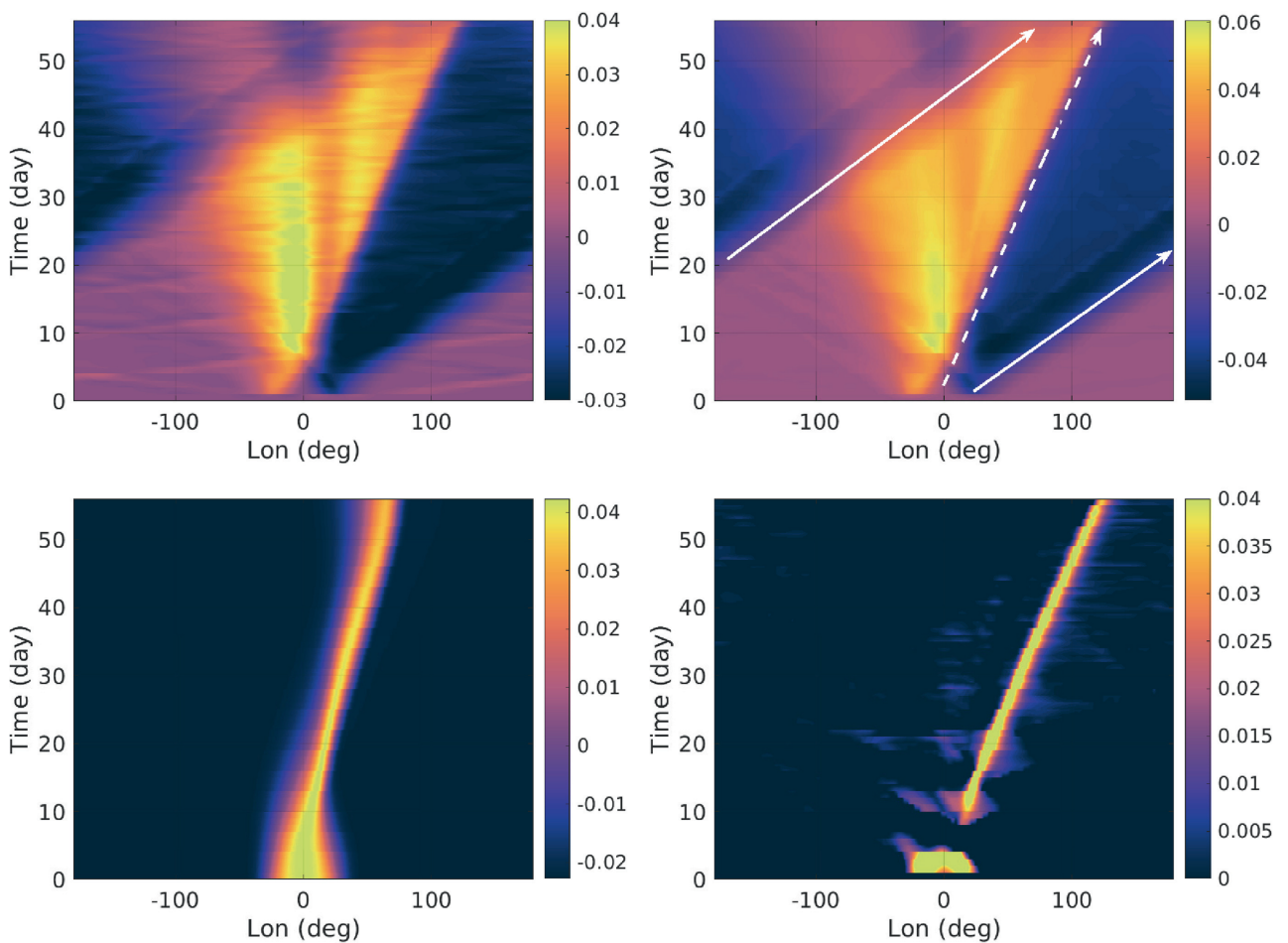


FIGURE 8 *Upper row:* Hovmöller diagram of zonal velocity in the lower layer (left panel) and the baroclinic zonal velocity at 0.2° latitude related to equatorial adjustment due to an initial positive buoyancy anomaly in a moist-convective environment. Solid and dashed arrows indicate the eastern and western fronts of BKW respectively. *Lower row:* Corresponding Hovmöller diagram of the buoyancy anomaly (left panel) and condensation (right panel) [Colour figure can be viewed at wileyonlinelibrary.com]

warm water in the western Indian Ocean, next to the East African Coastal Current (EACC), could be a plausible candidate for such a buoyancy anomaly. In this dual interaction case, the critical amplitude of b_1 can be much

smaller than that of the adjustment scenario with just the buoyancy anomaly alone (cf. left panel of Figure 5b). In other words, such interaction facilitates the triggering state of the new MJO-like structure. When the “hybrid

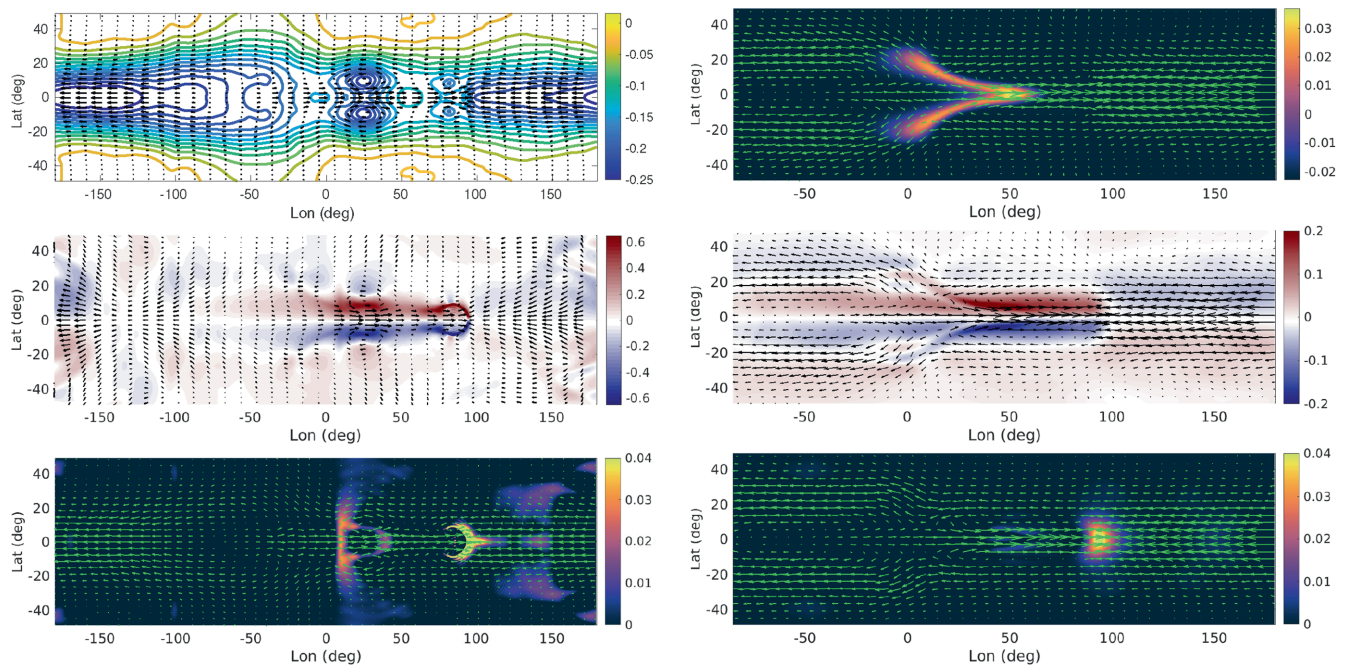


FIGURE 9 All left panels relate to eastward propagation of the “hybrid structure” as seen in one snapshot of the baroclinic thickness anomaly (colors, left column) and baroclinic velocity (arrows) (upper left panel), condensation pattern with baroclinic velocity field (middle left panel), and vorticity and velocity field in the lower layer (lower left panel), due to relaxation (adjustment) of a negative thickness anomaly in a moist-convective environment. All right panels relate to eastward propagation of the MJO-like structure due to equatorial adjustment of the large-scale localized buoyancy anomaly as seen in the buoyancy (colors, *upper left panel*) and velocity field (arrows). *Middle left panel*: Corresponding condensation (colors) and baroclinic velocity (arrows). *Lower panel*: Vorticity (colors) and velocity field (arrows) in the lower layer. Time = 44 [day] in moist-convective environment [Colour figure can be viewed at wileyonlinelibrary.com]

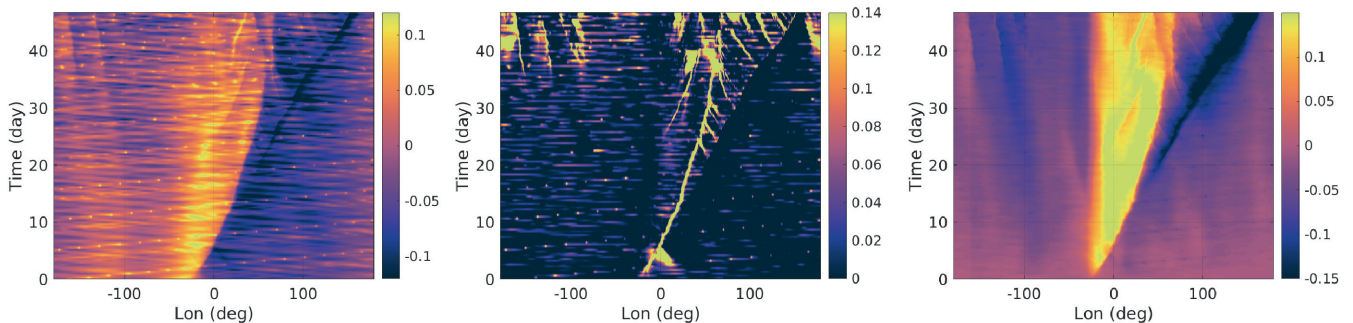


FIGURE 10 Hovmöller diagram of the zonal velocity (left panel), condensation (middle panel) in the lower layer, and the baroclinic zonal velocity (right panel) at 0.2° latitude because of passing BKW (at time = 0) over a positive buoyancy anomaly with half the intensity of the initial b_1 presented in the initial state of Figure 5b [Colour figure can be viewed at wileyonlinelibrary.com]

“structure” emerges from the thermo-geostrophic adjustment, both CCBKW and dipolar structure have interconnected eastward propagation; however, after about two weeks, CCBKW, due to its higher phase speed, produces a distinctive double rainband structure. The more extended the initial distribution of the b_1 anomaly, the later the occurrence of the double rainband structure. By approaching the suppressed stage of eastward propagation, the dipolar structure gradually loses its coherent structure and vorticity strength. After detachment, the BKW is

accelerated due to less moist convection and transition to a (semi-“dry” environment. The average phase speed of BKW in the Western Hemisphere is greater than that of the eastern one.

The other result of this study is that, in addition to amplitude, the zonal scale of the buoyancy perturbation needs to be of approximately the same order as that of BKW to induce MJO-like eastward propagation. If the perturbation scale is much smaller than that of BKW, then a fully adjusted, well-intensified vortex-pair structure

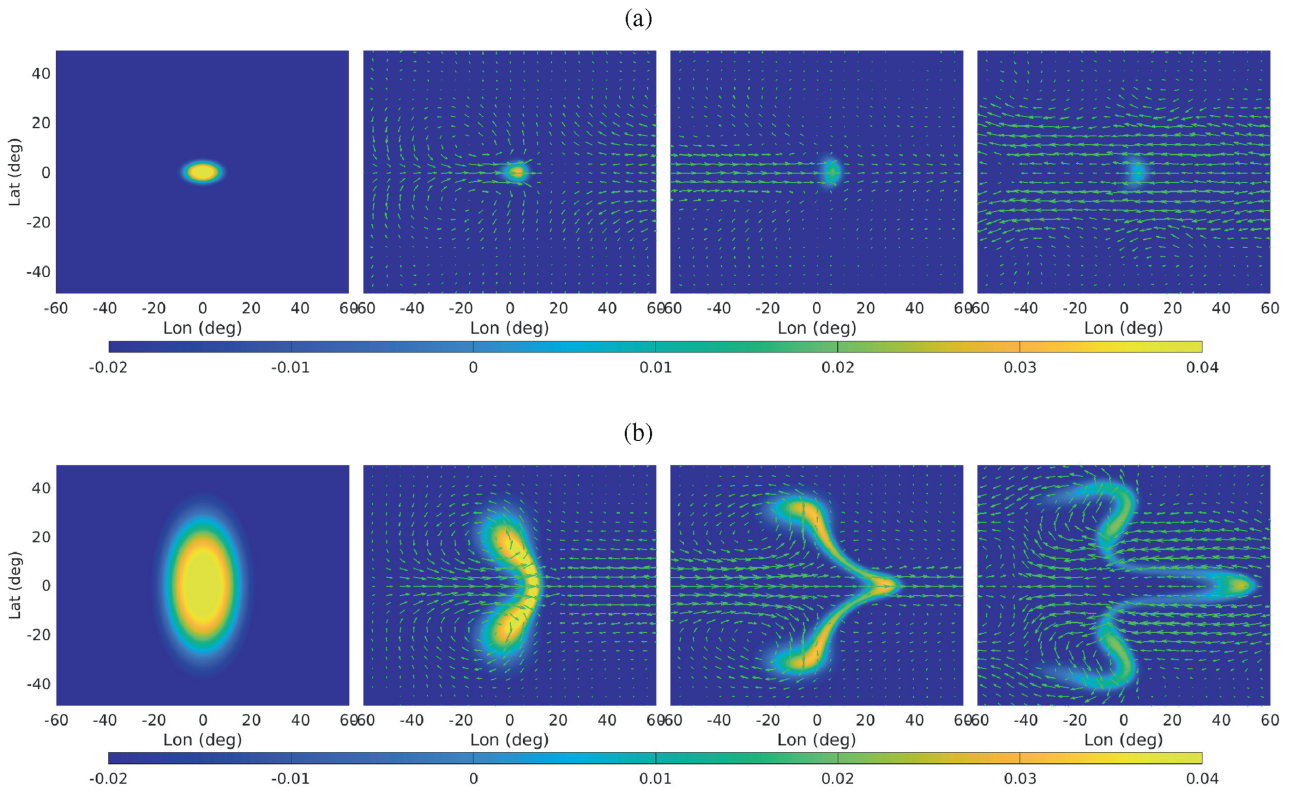


FIGURE 11 (a) Field of buoyancy perturbation (colors) in the lower layer and corresponding velocity field (arrows) from initial to late stages of equatorial adjustment in a moist-convective environment on a synoptic scale, and (b) large-scale meridionally elongated buoyancy perturbation. Time = 0, 10, 30, 50 [day], consecutively from left to right [Colour figure can be viewed at wileyonlinelibrary.com]

cannot develop fully, propagate eastward, and couple with BKW (Figure 11a). What we see is like what Gill's mechanism predicts. Consequently, BKW acquires its normal phase speed and is not slowed down. The late-stage evolution of a synoptic-scale buoyancy perturbation illustrates an eastward curved front. Evolution of a large-scale meridionally elongated buoyancy perturbation in the lower layer (b_1) illustrates that, if the meridional length-scale is much greater than that of BKW, then the modon loses its coherency. Consequently, the northern and southern vortices of the dipolar structure move to the northwest and southwest, respectively, and we see formation of a new dipolar structure on a smaller scale (Figure 11b). After the dissipation of the dipolar structure, b_1 reaches a ceased state of eastward propagation.

We repeated a similar equatorial adjustment of a positive buoyancy anomaly with realistic bottom topography (not shown) and found asymmetric behavior of the eastward propagation due to the interaction of large-scale motions with land. During the initial days of adjustment, there is a meridional shift of buoyancy to the Southern Hemisphere. This tendency can be ascribed to more enhanced moist convection in the southern sector of the Indian Ocean in comparison with the northern sector, which is covered by land at latitudes above 15°. The

dipolar component of the “hybrid structure” therefore rotates clockwise. As time goes on, buoyancy anomalies are dissipated and advected toward higher latitudes. A comprehensive study of adjustment scenarios, including land and topography, awaits further study.

4 | COMPARISON OF THE RESULTS WITH THE MJO

We summarize below some key features of the MJO episodes and their counterparts in our experiments.

- *Convective activity at the onset of MJO initiation*

A distinguishing feature of the MJO's genesis in comparison with other stages of its evolution is an abrupt transition of convective activity from the intertropical convergence zone (ITCZ) to the Equator (Chen *et al.*, 2016). The strong dry air intrusion from the extratropical regions reaches its maximum equatorward wind speed during the MJO's life cycle (Chen *et al.*, 2016). This phenomenon is consistent with what we observe in the genesis mechanism based on the aforementioned adjustment scenarios (cf. Figure 3).

According to in situ and satellite observations, transition from preconvective initiation to initiation stages of the MJO takes 2–20 days (Riley *et al.*, 2011; Xu and Rutledge, 2015). Within this broad time span, daytime growth of the areal coverage and depth of shallow, nonprecipitating cumulus clouds exists (Ruppert and Johnson, 2015). Some observations illustrate precursor signals associated with MJO convection initiation about 3–10 days prior to the initiation date as anomalous ascending motion, heat fluxes (cf. Li *et al.*, 2015; Xu and Rutledge, 2015), or enhanced humidity (Powell and Houze, 2014) in the lower troposphere. A remarkable coupling exists between moisture and convection, as seen from the wavenumbers and frequencies of the MJO episodes (Yasunaga and Mapes, 2012). This sort of preconvective signal in our simulations can be seen consistently from initial adjustment that is associated with a gradual increase of humidity or a transition to deep convection, shown as abrupt growth of condensation within the initial days of adjustment (Figures 6 and 8). Enhanced convective activity is a necessary condition for evolution of MJO-like structures by equatorial adjustment, as seen in the comparison of “dry” versus moist-convective evolution (Figures 4c and 5) that occurs in the vicinity of the center of the depressed zone or positive buoyancy anomaly. Transition to the onset of MJO initiation over the Indian Ocean is associated with deep cloudiness, enhanced convective activity, a series of quasistationary deep heating anomalies, and low-level moisture convergence (e.g. Hsu *et al.*, 1990; Matthews and Kiladis, 1999; Kemball-Cook and Weare, 2001; Hsu and Lee, 2005; Seo and Kumar, 2008; Zhang and Ling, 2012; Straub, 2013). Figure 6 presents a peak level of condensation in the initial stages of the phase-speed transition. A wacky look at this figure shows that two peaks exist in the genesis stages of the MJO-like structure: (1) at the very beginning of the adjustment, before formation of dipolar structure due to the high convergent zone, and (2) when the tower of elliptical condensation collapses toward the center and moves to the east, as shown in the first and second panels of Figures 4 and 5d. A repetitive pattern of a deep tropopause-penetrating convective process, which happens about one week before the main MJO peak in convection, has been observed via *Cloud-Aerosol Lidar and Infrared Pathfinder Satellite Observations* (CALIPSO; Genio *et al.*, 2012). Our simulations reveal a similar pattern, as seen, for example, in the Hovmöller diagram of condensation (Figure 8). Some other observations also show a similar rapid lofting of moisture into the middle troposphere at the onset of deep convection (Kiladis *et al.*, 2005). It is worth noting that progression from shallow to deep convection on

many time-scales or moisture transition is not unique to the MJO. It exists in almost all tropical convective systems (Mapes *et al.*, 2006; Kiladis *et al.*, 2009).

- *Quadrupolar structure and enhanced dipolar structure*

Quadrupole structure with an opposite-sign vorticity anomaly in the upper layer is known as one of the key observational facts of MJO events (Rui and Wang, 1990; Kiladis *et al.*, 2005; Wang *et al.*, 2019). The dominance of the rear dipolar structure is well documented in the literature (e.g. Lau and Phillips, 1986; Matthews, 2000; Zhang and Ling, 2012; Wang *et al.*, 2019). Our results illustrate that at the onset of adjustment we observe a similar structure and in the early stages an opposite sign of vorticity in the upper troposphere. This structure is zonally asymmetric, because the western sector of this quadrupole is occupied by the dipole, while the eastern sector is inhabited by the CCBKW (Figure 4). Consequently, the zonal velocity field toward the center of the “hybrid structure” is also opposite in the two layers, particularly around the CCBKW. In observations, MJO events are accompanied by a forced component of hybrid Rossby–Kelvin type (cf. Hendon and Salby, 1994; Dunkerton and Crum, 1995). We see smooth detachment of the CCBKW in simulations of this study (cf. Figure 7). A similar pattern has been observed and analyzed by Sobel and Kim (2012). Our simulations reveal the nonuniformity of the “hybrid structure” and its deformation from genesis to suppression stages. One of these deformations is a zonal spread of the velocity field due to westward and eastward pulling of Rossby waves and KWs (Figures 7 and 9), which resembles the observed evolution of the MJO (Kiladis *et al.*, 2005). All the simulations (cf. Figures 3 and 5b–d) illustrate that CCBKW is dominant in the east of the central convective envelope, which agrees with data analysis of tropical wave activity (Straub and Kiladis, 2003).

- *Propagation speed versus Kelvin-wave phase velocity*

The slow eastward propagation speed of the MJO ($\approx 5 \text{ m}\cdot\text{s}^{-1}$) may be its the most dominant feature that does not exist in other equatorial waves (cf. Weickmann *et al.*, 1985; Knutson *et al.*, 1986; Wheeler and Kiladis, 1999; Wheeler and Hendon, 2004). As revealed by Figures 7 and 8, we observe two distinguished eastward velocity fronts in the Hovmöller diagram of baroclinic zonal velocity. The slower one is for the dipolar structure, which has the same order as the MJO phase speed, while the other indicates the CCBKW with phase speed $\approx 12 \text{ m}\cdot\text{s}^{-1}$, which agrees with observations exhibiting a range of $\approx 10\text{--}17 \text{ m}\cdot\text{s}^{-1}$ (e.g. Hendon and Salby, 1994; Wheeler and Kiladis, 1999; Straub and Kiladis, 2002). Initial conditions, such as the spatial distribution of anomalies, thickness of layers, strength of

Newtonian cooling, and stratification of layers, θ_2/θ_1 , are factors that lead to slight variation of CCBKW phase speed. Intensive moist convection and latent heat release decrease the phase velocity of CCBKWs (Figure 3) at the onset of baroclinic adjustment, which corresponds to the active phase of MJO initiation. Slowed down CCBKW is one of the key components of “*hybrid structure*”. Observations also present that phase speeds of associated CCBKWs during the active phase over the Indian Ocean are smaller than those of suppressed phases over the eastern Pacific Ocean, where the MJO convection has almost ceased (Madden and Julian, 1972; Hendon and Salby, 1994; Milliff and Madden, 1996; Weickmann *et al.*, 1997; Matthews, 2000; Sperber, 2003; Roundy, 2008).

- *Precipitation patterns and westerly and easterly inflows*

The center of the “*hybrid structure*”, between the dipole and CCBKW, is the most convergent zone and is denoted as the main condensation zone, particularly in the initial stages (cf. patterns of condensation in Figures 4c, 5d, and 9), which is consistent with precipitation in the MJO structure (Zhang, 2005). Regions of dense and depleted humidity have been observed to the east and west of the hybrid’s center (e.g. Sperber, 2003; Kiladis *et al.*, 2005; Adamec and Wallace, 2015). Such a distribution of water vapor is consistent with the condensation and divergence fields of the “*hybrid structure*” (Figure 4c). The typical swallowtail pattern of precipitation, which is common for the MJO during active phases (Zhang and Ling, 2012; Adamec and Wallace, 2015), is consistent with snapshots of condensation (Equation 9).

Low level (≈ 850 -hPa) westerlies and easterlies in the western and eastern sectors of the “*hybrid structure*” are frequently observed characteristics of the MJO (Madden, 1986; Sperber, 2003; Zhang, 2005). The MJO includes a stiff wind over an area roughly 1,500 km in latitude and 4,500 km in longitude. The MJO has a great impact on both tropical moist-air circulation and midlatitude intraseasonal environment variables (Vitart and Molteni, 2010). Figures 4, 7, and 9 indicate a similar pattern of westerlies and easterlies with the same order of magnitude. Our results reveal that, by diminishing the strength of moist convection, there will be a gap between the dipolar structure and CCBKW that is filled up by weak westerlies (Figures 7 and 9). In this case the detachment is accompanied by a distinctive double rainband structure. One of these structures moves with the CCBKW, so its phase speed is in the range of that of CCBKWs. Some similar precipitation patterns have been documented by Chen *et al.* (2016) and Zhu and Li (2017). Let us note that condensation in

this version of the mcTRSW model is synonymous with precipitation and presents large-scale deep convection.

- *Potential temperature anomaly in MJO episodes*

A steadily daily-averaged increase in sea-surface temperature (SST) prior to the active phase of the MJO and gradual slowing down of the SST during eastward propagation have been reported in observational studies (cf. Vialard *et al.*, 2008; Matthews *et al.*, 2014; Moum *et al.*, 2014; Chen *et al.*, 2016). SST is not included in our stand-alone version of the model directly. If we assume that the buoyancy field in the initial step is affected by the SST, then Figures 5 and 9 will illustrate the evolution of the localized disturbance of atmospheric buoyancy in the lower layer. Figure 9 apparently shows that there is a lag between eastward propagation of the convective zone, illustrated as condensation, and the potential temperature anomaly. A similar lag has been observed; for instance, Hendon and Glick (1997) reported that spatially coherent SST anomalies propagate eastward in the Indian Ocean along with the large-scale convective anomaly, but with a 1/4 cycle lag.

- *Sub/mesoscale convective envelopes of high buoyancy at late stages*

One of the dominant processes that has a remarkable impact in destabilizing the eastward propagation and genesis of cyclones at late stages is collision of circumnavigated CCBKW into it. As is clearly visible through Hovmöller diagrams (Figures 7 and 8), this destabilization not only diminishes the total eastward-propagating time span but also engenders a few convective events with smaller spatial scale and longevity that propagate westward, as is easily visible at late stages of Hovmöller diagrams. In real MJO events, although detachment of smaller-scale low-frequency convective envelopes has been observed from the onset of the MJO’s active phase as detachment of a westward-propagating cloud cluster of order 100 km (Leary and Houze, 1979) from a large-scale super cluster (Nakazawa, 1988), at late stages the number of envelopes is increasing and some of these small convective envelopes can merge and form tropical storms in the western Pacific (Straub and Kiladis, 2003). The formation of similar low-frequency tropical cyclones in the eastern Pacific is ascribed as more likely due to MJO-related episodes with lower-tropospheric westerly anomalies (Maloney and Hartmann, 2000). According to Maloney and Hartmann (2000), westerly (easterly) equatorial wind anomalies in the lower troposphere are accompanied by enhanced (suppressed) convection over the eastern Pacific hurricane region.

- *Recurrent generation and episodic versus periodic character of the MJO*

Each spatial distribution and amplitude of b_1 generates a “hybrid structure” that has its own longevity, appearance, and periodicity of the MJO-like structure (Figure 11), even though the underlying mechanism for each episode is the same. The intensity and extension of diabatic processes associated with the coupled structures in each episode and consequently the amount of deceleration of BKW are not exactly the same. Thus, it is no wonder that the MJO is not strictly an oscillation but an episodic severe weather event (Hartmann and Hendon, 2007).

The aforementioned mechanism for the recurrent generation of MJO-like structure (Section 3) also gives a plausible explanation for various studies that have documented the connection of BKW to the next MJO event and its role in activating convection of the next cycle of the MJO once BKW enters over the warm water in the western Indian Ocean next to the EACC (cf. Knutson and Weickmann, 1987; Kikuchi and Takayabu, 2003).

5 | CONCLUSION AND DISCUSSION

By means of a new pseudo-spectral multilayer mcTRSW model in a full sphere that uses spin-weighted spherical harmonics, we extended the MJO mechanism previously proposed by Rostami and Zeitlin (2020a). In this study, potential temperature variation, which was the missing part of the mcTRSW model used by Rostami and Zeitlin (2020a), is implemented in the mcTRSW model in a full sphere. In contrast to the classical setup of shallow-water models, gradients of the vertically averaged potential temperature and density are variant in the mcTRSW model. Therefore, in addition to studying the baroclinic evolution of the relaxation of large-scale localized warming due to a negative pressure anomaly over the equatorial zone, we could examine the explicit evolution of a buoyancy anomaly. We found an equatorial adjustment beyond Gill’s mechanism (Gill, 1980) for the genesis and backbone structure of an eastward-propagating MJO-like structure. According to this theory, an eastward-moving structure can be generated in a self-sustained and self-propelled manner whenever the spatial scale and amplitude of the buoyancy anomaly or negative pressure anomaly or both reach a critical threshold state in the lower troposphere in the presence of moist convection. The excited system has a “hybrid structure” that is constituted by a combination of a “quasi-equatorial modon” and a CCBKW. The latter has greater phase speed than the former. This coupling lasts for

an intraseasonal period. This mechanism captures most of the crudest features of the MJO during the genesis, early, and late stages of its evolution in the lower and upper troposphere, as seen in the convective activity, quadrupolar structure, vorticity fields, wave activity, phase speed, westerly and easterly inflows, condensation pattern, and intraseasonal lifespan in an obvious manner. Inclusion of the buoyancy term in the mcTRSW model enhances the coupling between dynamics and convection and hence yields a more realistic evolution of the “hybrid structure”. We examined the same adjustment scenarios with real bottom topography as well, and we found that the crudest features of the aforementioned adjustment mechanism for generation of the “hybrid structure” are robust.

Another important question that we addressed in the present article is a possible mechanism for the recurrent generation of the next cycle of the MJO. At the late stages of evolution of the “hybrid structure”, the BKW becomes less strongly attached to dipolar structure and convection. Thus, it finally becomes detached and continues its circumnavigation all around the Equator with greater phase speed in (semi-) dry air. When the circumnavigated BKW, with intraseasonal periodicity, interacts with a new disturbance of the large-scale buoyancy anomaly, a new eastward-propagating “hybrid structure” emerges from thermo-geostrophic adjustment. The warm water in the western Indian Ocean, next to the EACC, can provide such large-scale buoyancy anomalies. Furthermore, the higher phase speed of the CCBKW with respect to that of the dipolar structure may yield double condensation fronts during the separation stage in the presence of moist air.

In the present study, we also found a mechanism to explain the small-scale turbulence that appears in the late stages of simulations; that is, collision of the circumnavigating convectively coupled BKW with a slow-evolving remaining part of the perturbation. This collision is accompanied by subsequent destabilization of the vorticity shear and/or convective small-scale instabilities of an elongated potential temperature front. It is worth mentioning that collision of the circumnavigated BKW with a large-scale positive buoyancy anomaly can trigger new eastward propagation of the “hybrid structure” that may explain the intraseasonal periodicity of MJO episodes. Successive interactions of the eastward-moving “hybrid structure” with IGW, barotropic KW, and also thermal cooling have a destructive impact on coherency and a deceleration effect on the phase speed of the “hybrid structure” that lead to the generation of many small-scale disturbances. The aforementioned adjustment scenarios could also explain the appearance of the double rainband structures that have been observed in some MJO episodes as detachment of CCBKW from the dipolar structure in a weak moist-convective environment.

The observed mechanism in our model could provide some supplementary explanations for some existing theories. In this respect, it encompasses some theories that previously seemed divergent. For instance, the “*hybrid structure*” supports the existence of an equatorial modon or planetary-scale solitary Rossby-vortex pair in the MJO (cf. Yano and Tribbia, 2017) as a large-scale tropical circulation that is nondivergent to leading order. The dipolar structure can maintain its coherency and eastward propagation in the absence of dissipation and baroclinicity, even in a “dry” environment. Moist convection is a necessary condition for the genesis of the “*hybrid structure*”, at least in the early stages of equatorial adjustment. Moist convection in this mechanism yields slowed-down zonal propagation of CCBKW as well. By illustrating that a combined “*hybrid structure*” yields similar slowed-down propagation of CCBKW via moist convection, the results of the present study support theories that include a slowed-down Kelvin wave as a core component of the MJO’s structure, e.g. Kim and Zhang (2021), who produced a slowed-down Kelvin wave by including momentum damping in the linear equatorial shallow-water equations in a “dry” environment. Although the results in this article reveal high degrees of convergence with theories that include a mixed Kelvin–Rossby wave structure (e.g., Wang *et al.*, 2016 and references therein), there is a hermeneutic difference between the quasi-equatorial modon with eastward propagation and Rossby waves with westward propagation in the western sector of the MJO-like structure. The vortex-pair structure in our model emerges as a modon-like structure beyond Gill’s mechanism when a buoyancy anomaly, depressed pressure, or a combination of both reaches a triggering state, while the theories based on mixed Kelvin–Rossby wave structure follow Gill’s mechanism. The vorticity of the vortex pair in a modon-like structure is more intensified than that of a Rossby wave in Gill’s mechanism. Capturing the full nonlinear evolution of the variables is another difference of our proposed mechanism from those of linear wave theories (cf. Fuchs and Raymond, 2017) that helps us to simulate more features of the MJO-like structure, like a well-intensified vortex pair, for the reason that, according to basic knowledge of wave theory, the phase speed of an equatorial modon, in its ideal form, is outside the range of speeds for a linear Rossby wave of any zonal scale (cf. Osborne, 1991; Grimshaw and Iooss, 2003). Namely, Rossby waves need to be identified in the wavenumber–frequency phase space outside the range of linear wave dispersion to propagate eastward (Yano and Tribbia, 2017). Moreover, in the Tropics, the magnitude of the Rossby number of atmospheric motion is typically one order greater than in mid and high latitudes; therefore, the nonlinear effect of advection becomes more important (Maicun, 1987). In moist

wave theories (cf. Adames and Kim, 2016) eastward propagation is due mainly to meridional advection of mean moisture by MJO winds. In such moist wave theories, a prognostic moisture anomaly exists in the parameterization of the boundary layer and a passive Gill-like response. However, in the proposed model in this study there is no need for prognostic moisture. Moisture-fed convection provides a mechanism for the “*hybrid structure*” to be excited and maintained. This mechanism differs fundamentally from that of moisture-mode theories, in which no similar “dry” dynamical basic structure exists. The barotropic equatorial modon and BKWs have innate eastward propagation even in a “dry” environment. By growing baroclinicity in the equatorial modon, we observe loss of coherency and an arrest of eastward propagation (Rostami and Zeitlin, 2020b).

This study aims at understanding the fundamental dynamics of the MJO. Thus, some features of the MJO, such as details of the vertical structure, full boundary effects of the maritime continent, effects of bottom topography, direct effects of SST, and influence of radiative transfer have not been captured by this hierarchy of the model; nevertheless, these features can be investigated by more complex versions of the model. This model, with its intermediate complexity, is also the dynamical core of Aeolus2, one of the atmospheric models of the Potsdam Earth Model (POEM). This model has the capability to capture thermal and dynamical effects of orography and radiative transfer distinctively with physically reasonable asymptotic limits. Via relaxation of the potential temperature of the air to SST, the model is able to be linked to SST variation of an oceanic model. As model Aeolus2 is based on minimal parametrization, it can be used for testing general circulation models too.

AUTHOR CONTRIBUTIONS

Masoud Rostami: conceptualization; data curation; formal analysis; investigation; methodology; project administration; resources; software; validation; visualization; writing – original draft; writing – review and editing. **Bowen Zhao:** data curation; formal analysis; investigation; methodology; software; validation; writing – review and editing. **Stefan Petri:** data curation; methodology; resources; software; writing – review and editing.

ACKNOWLEDGEMENTS

We are grateful to Vladimir Zeitlin for supporting the derivation of the multilayer TRSW model and reviewing the article, Stefan Rahmstorf and Georg Feulner for stimulating discussions, and two anonymous reviewers for valuable comments that helped clarify several aspects of the original article. This research was partially funded

by H&M Foundation (project ID: 20A048). Open Access funding enabled and organized by Projekt DEAL.

CONFLICT OF INTEREST

The authors report no conflict of interest.

ORCID

Masoud Rostami  <https://orcid.org/0000-0003-1730-5145>

Stefan Petri  <https://orcid.org/0000-0002-4379-4643>

REFERENCES

Adamec, A. and Wallace, J. (2015) Three-dimensional structure and evolution of the moisture field in the MJO. *Journal of the Atmospheric Sciences*, 72, 3733–3754.

Adames, A.F. and Kim, D. (2016) The MJO as a dispersive, convectively coupled moisture wave: theory and observations. *Journal of the Atmospheric Sciences*, 73(3), 913–941.

Beron-Vera, F. (2021) Multilayer shallow-water model with stratification and shear. *Revista Mexicana de Fisica*, 67(3), 351–364.

Betts, A. and Miller, M. (1986) A new convective adjustment scheme. Part II: single column tests using GATE wave, BOMEX, ATEX and arctic air-mass data sets. *Quarterly Journal of the Royal Meteorological Society*, 112, 693–762.

Bouchut, F., Lambaerts, J., Lapeyre, G. and Zeitlin, V. (2009) Fronts and nonlinear waves in a simplified shallow-water model of the atmosphere with moisture and convection. *Physics of Fluids*, 21(11), 116604.

Boyd, J.P. and Yu, F. (2011) Comparing seven spectral methods for interpolation and for solving the Poisson equation in a disk: Zernike polynomials, Logan-Shepp ridge polynomials, Chebyshev-Fourier series, cylindrical Robert functions, Bessel-Fourier expansions, square-to-disk conformal mapping and radial basis functions. *Journal of Computational Physics*, 230(4), 1408–1438.

Charney, J. (1963) A note on large-scale motions in the tropics. *Journal of the Atmospheric Sciences*, 20, 607–609.

Chen, S.S., Kerns, B.W., Guy, N., Jorgensen, D.P., Delano, J., Viltard, N., Zappa, C.J., Judt, F., Lee, C.-Y. and Savarin, A. (2016) Aircraft observations of dry air, the ITCZ, convective cloud systems, and cold pools in MJO during DYNAMO. *Bulletin of the American Meteorological Society*, 97(3), 405–423.

Chertock, A., Kurganov, A. and Liu, Y. (2014) Central-upwind schemes for the system of shallow water equations with horizontal temperature gradients. *Numerische Mathematik*, 127(4), 595–639.

Dunkerton, T.J. and Crum, F.X. (1995) Eastward propagating 10–15-day equatorial convection and its relation to the tropical intraseasonal oscillation. *Journal of Geophysical Research*, 100(D12), 25781–25790.

Flierl, G., Larichev, V., McWilliams, J. and Reznik, G. (1980) The dynamics of baroclinic and barotropic solitary eddies. *Dynamics of Atmospheres and Oceans*, 5(1), 1–41.

Fuchs, Z. and Raymond, D.J. (2005) Large-scale modes in a rotating atmosphere with radiative-convective instability and WISHE. *Journal of the Atmospheric Sciences*, 62(11), 4084–4094.

Fuchs, Z. and Raymond, D.J. (2017) A simple model of intraseasonal oscillations. *Journal of Advances in Modeling Earth Systems*, 9(2), 1195–1211.

Fuchs-Stone, Z. (2020) WISHE-moisture mode in a vertically resolved model. *Journal of Advances in Modeling Earth Systems*, 12(2), e2019MS001839.

Fuchs-Stone, Z. and Emanuel, K. (2022) Sensitivity of linear models of the Madden-Julian oscillation to convective representation. *Journal of the Atmospheric Sciences*, 79(6), 1575–1584.

Gelfand, I.M. and Shapiro, Z.Y. (1956) Representations of the group of rotations in three-dimensional space and their applications. *American Mathematical Society Translations*, 2, 207–316.

Genio, A.D.D., Chen, Y., Kim, D. and Yao, M.-S. (2012) The MJO transition from shallow to deep convection in CloudSat/CALIPSO data and GISS GCM simulations. *Journal of Climate*, 25(11), 3755–3770.

Gill, A. (1980) Some simple solutions for heat induced tropical circulation. *Quarterly Journal of the Royal Meteorological Society*, 106, 447–462.

Gill, A. (1982) Studies of moisture effects in simple atmospheric models: the stable case. *Geophysical and Astrophysical Fluid Dynamics*, 19, 119.

Grimshaw, R. and Iooss, G. (2003) Solitary waves of a coupled Korteweg-de Vries system. *Mathematics and Computers in Simulation*, 62(1), 31–40. Nonlinear Waves: Computation and Theory II.

Hartmann, D.L. and Hendon, H.H. (2007) Resolving an atmospheric enigma. *Science*, 318(5857), 1731–1732.

Hendon, H.H. and Glick, J. (1997) Intraseasonal air-sea interaction in the tropical Indian and Pacific Oceans. *Journal of Climate*, 10(4), 647–661.

Hendon, H.H. and Salby, M.L. (1994) The life cycle of the Madden-Julian oscillation. *Journal of the Atmospheric Sciences*, 51(15), 2225–2237.

Hoskins, B.J. and Bretherton, F.P. (1972) Atmospheric frontogenesis models: mathematical formulation and solution. *Journal of the Atmospheric Sciences*, 29(1), 11–37.

Hsu, H.-H., Hoskins, B.J. and Jin, F.-F. (1990) The 1985/86 intraseasonal oscillation and the role of the extratropics. *Journal of the Atmospheric Sciences*, 47(7), 823–839.

Hsu, H.-H. and Lee, M.-Y. (2005) Topographic effects on the eastward propagation and initiation of the Madden-Julian oscillation. *Journal of Climate*, 18(6), 795–809.

Jiang, X., Adames, A.F., Kim, D., Maloney, E.D., Lin, H., Kim, H., Zhang, C., DeMott, C.A. and Klingaman, N.P. (2020) Fifty years of research on the Madden-Julian oscillation: recent progress, challenges, and perspectives. *Journal of Geophysical Research: Atmospheres*, 125(17), e2019JD030911.

Katsaros, K. (2001) Evaporation and humidity. In: Steele, J.H. (Ed.) *Encyclopedia of Ocean Sciences*. Oxford: Academic Press, pp. 870–877.

Kemball-Cook, S.R. and Weare, B.C. (2001) The onset of convection in the Madden-Julian Oscillation. *Journal of Climate*, 14(5), 780–793.

Kikuchi, K. and Takayabu, Y.N. (2003) Equatorial circumnavigation of moisture signal associated with the Madden-Julian Oscillation (MJO) during boreal winter. *Journal of the Meteorological Society of Japan Series II*, 81(4), 851–869.

Kiladis, G.N., Straub, K.H. and Haertel, P.T. (2005) Zonal and vertical structure of the Madden–Julian oscillation. *Journal of the Atmospheric Sciences*, 62(8), 2790–2809.

Kiladis, G.N., Wheeler, M.C., Haertel, P.T., Straub, K.H. and Roundy, P.E. (2009) Convectively coupled equatorial waves. *Reviews of Geophysics*, 47(2), RG2003. <https://doi.org/10.1029/2008RG000266>.

Kim, J.-E. and Zhang, C. (2021) Core dynamics of the MJO. *Journal of the Atmospheric Sciences*, 78(1), 229–248.

Knutson, T.R. and Weickmann, K.M. (1987) 30–60 day atmospheric oscillations: composite life cycles of convection and circulation anomalies. *Monthly Weather Review*, 115(7), 1407–1436.

Knutson, T.R., Weickmann, K.M. and Kutzbach, J.E. (1986) Global-scale intraseasonal oscillations of outgoing longwave radiation and 250 mb zonal wind during Northern Hemisphere summer. *Monthly Weather Review*, 114(3), 605–623.

Kurganov, A., Liu, Y. and Zeitlin, V. (2020) Moist-convective thermal rotating shallow water model. *Physics of Fluids*, 32(6), 066601.

Kurganov, A., Liu, Y. and Zeitlin, V. (2021a) Interaction of tropical cyclone-like vortices with sea-surface temperature anomalies and topography in a simple shallow-water atmospheric model. *Physics of Fluids*, 33(10), 106606.

Kurganov, A., Liu, Y. and Zeitlin, V. (2021b) Thermal versus isothermal rotating shallow water equations: comparison of dynamical processes by simulations with a novel well-balanced central-upwind scheme. *Geophysical and Astrophysical Fluid Dynamics*, 115(2), 125–154.

Lahaye, N. and Zeitlin, V. (2016) Understanding instabilities of tropical cyclones and their evolution with a moist convective rotating shallow-water model. *Journal of the Atmospheric Sciences*, 73(2), 505–523.

Lambaerts, J., Lapeyre, G. and Zeitlin, V. (2011a) Moist versus dry barotropic instability in a shallow-water model of the atmosphere with moist convection. *Journal of the Atmospheric Sciences*, 68, 1234–1252.

Lambaerts, J., Lapeyre, G. and Zeitlin, V. (2012) Moist versus dry baroclinic instability in a simplified two-layer atmospheric model with condensation and latent heat release. *Journal of the Atmospheric Sciences*, 69, 1405–1426.

Lambaerts, J., Lapeyre, G., Zeitlin, V. and Bouchut, F. (2011b) Simplified two-layer models of precipitating atmosphere and their properties. *Physics of Fluids*, 23(4), 046603.

Larichev, V. and Reznik, G. (1976) Two-dimensional solitary Rossby waves. *Doklady USSR Academy of Sciences*, 231, 1077–1080.

Lau, K.M. and Phillips, T.J. (1986) Coherent fluctuations of extratropical geopotential height and tropical convection in intraseasonal time scales. *Journal of the Atmospheric Sciences*, 43(11), 1164–1181.

Lavoie, R.L. (1972) A mesoscale numerical model of lake-effect storms. *Journal of the Atmospheric Sciences*, 29(6), 1025–1040.

Leary, C. and Houze, R. (1979) The structure and evolution of convection in a tropical cloud cluster. *Journal of the Atmospheric Sciences*, 36, 437–457.

Lecoanet, D., Vasil, G.M., Burns, K.J., Brown, B.P. and Oishi, J.S. (2019) Tensor calculus in spherical coordinates using Jacobi polynomials. Part-II: implementation and examples. *Journal of Computational Physics*, 3, 100012.

Li, T., Zhao, C., Hsu, P. and Nasuno, T. (2015) MJO initiation processes over the tropical Indian Ocean during DYNAMO/CINDY2011. *Journal of Climate*, 28(6), 2121–2135.

Liang, Y., Fedorov, A.V., Zeitlin, V. and Haertel, P. (2021) The excitation of the Madden–Julian oscillation in atmospheric adjustment to equatorial heating. *Journal of the Atmospheric Sciences*, 78(12), 3933–3950.

Madden, R.A. (1986) Seasonal variations of the 40–50 day oscillation in the tropics. *Journal of the Atmospheric Sciences*, 43(24), 3138–3158.

Madden, R.A. and Julian, P.R. (1972) Description of global-scale circulation cells in the tropics with a 40–50 day period. *Journal of the Atmospheric Sciences*, 29(6), 1109–1123.

Madden, R.A. and Julian, P.R. (1994) Observations of the 40–50-day tropical oscillation: review. *Monthly Weather Review*, 122(5), 814–837.

Maicun, L. (1987) Equatorial solitary waves of tropical atmospheric motion in shear flow. *Advances in Atmospheric Sciences*, 4(2), 125–136.

Maloney, E.D. and Hartmann, D.L. (2000) Modulation of eastern North Pacific hurricanes by the Madden–Julian oscillation. *Journal of Climate*, 13(9), 1451–1460.

Mapes, B., Tulich, S., Lin, J. and Zuidema, P. (2006) The mesoscale convection life cycle: building block or prototype for large-scale tropical waves? *Dynamics of Atmospheres and Oceans*, 42(1–4), 3–29.

Matsuno, T. (1966) Quasi-geostrophic motions in the equatorial area. *Journal of the Meteorological Society of Japan*, 44, 25–43.

Matthews, A.J. (2000) Propagation mechanisms for the Madden–Julian oscillation. *Quarterly Journal of the Royal Meteorological Society*, 126(569), 2637–2651.

Matthews, A.J., Baranowski, D.B., Heywood, K.J., Flatau, P.J. and Schmidtko, S. (2014) The surface diurnal warm layer in the Indian Ocean during CINDY/DYNAMO. *Journal of Climate*, 27(24), 9101–9122.

Matthews, A.J. and Kiladis, G.N. (1999) The tropical-extratropical interaction between high-frequency transients and the Madden–Julian oscillation. *Monthly Weather Review*, 127(5), 661–677.

Milliff, R.F. and Madden, R.A. (1996) The existence and vertical structure of fast, eastward-moving disturbances in the equatorial troposphere. *Journal of the Atmospheric Sciences*, 53(4), 586–597.

Moum, J.N., de Szoeke, S.P., Smyth, W.D., Edson, J.B., DeWitt, H.L., Moulin, A.J., Thompson, E.J., Zappa, C.J., Rutledge, S.A., Johnson, R.H. and Fairall, C.W. (2014) Air-sea interactions from westerly wind bursts during the November 2011 MJO in the Indian Ocean. *Bulletin of the American Meteorological Society*, 95(8), 1185–1199.

Nakazawa, T. (1988) Tropical Super clusters within intraseasonal variations over the western Pacific. *Journal of the Meteorological Society of Japan Series II*, 66(6), 823–839.

Osborne, A.R. (1991) *Nonlinear topics in ocean physics*. Amsterdam & New York: Elsevier.

Powell, S. and Houze, R.A. (2014) The cloud population and onset of the Madden–Julian oscillation over the Indian Ocean during DYNAMO-AMIE. *Journal of Geophysical Research*, 118, 11979–11995.

Riley, E.M., Mapes, B.E. and Tulich, S.N. (2011) Clouds associated with the Madden–Julian oscillation: a new perspective from CloudSat. *Journal of the Atmospheric Sciences*, 68(12), 3032–3051.

Ripa, P. (1993) Conservation laws for primitive equations models with inhomogeneous layers. *Geophysical and Astrophysical Fluid Dynamics*, 70(1–4), 85–111.

Ripa, P. (1995) On improving a one-layer ocean model with thermodynamics. *Journal of Fluid Mechanics*, 303, 169–201.

Ripa, P. (1996) Low frequency approximation of a vertically averaged ocean model with thermodynamics. *Revista Mexicana de Física*, 42(1), 117–135.

Rong, P.-P. and Waugh, D.W. (2004) Vacillations in a shallow-water model of the stratosphere. *Journal of the Atmospheric Sciences*, 61(10), 1174–1185.

Rostami, M. and Zeitlin, V. (2017) Influence of condensation and latent heat release upon barotropic and baroclinic instabilities of atmospheric vortices in a rotating shallow water model on the *f*-plane. *Geophysical and Astrophysical Fluid Dynamics*, 111, 1–31.

Rostami, M. and Zeitlin, V. (2018) An improved moist-convective rotating shallow-water model and its application to instabilities of hurricane-like vortices. *Quarterly Journal of the Royal Meteorological Society*, 144(714), 1450–1462.

Rostami, M. and Zeitlin, V. (2019a) Eastward-moving convection-enhanced modons in shallow water in the equatorial tangent plane. *Physics of Fluids*, 31, 021701.

Rostami, M. and Zeitlin, V. (2019b) Geostrophic adjustment on the equatorial beta-plane revisited. *Physics of Fluids*, 31(8), 081702.

Rostami, M. and Zeitlin, V. (2020a) Can geostrophic adjustment of baroclinic disturbances in the tropical atmosphere explain mjo events? *Quarterly Journal of the Royal Meteorological Society*, 146(733), 3998–4013.

Rostami, M. and Zeitlin, V. (2020b) Eastward-moving equatorial modons in moist-convective shallow-water models. *Geophysical and Astrophysical Fluid Dynamics*, 115(3), 345–367.

Rostami, M. and Zeitlin, V. (2020c) Evolution, propagation and interactions with topography of hurricane-like vortices in a moist-convective rotating shallow-water model. *Journal of Fluid Mechanics*, 902, A24.

Rostami, M. and Zeitlin, V. (2022) Evolution of double-eye wall hurricanes and emergence of complex tripolar end states in moist-convective rotating shallow water model. *Physics of Fluids*, 34(6), 066602.

Rostami, M., Zeitlin, V. and Montabone, L. (2018) On the role of spatially inhomogeneous diabatic effects upon the evolution of Mars annular polar vortex. *Icarus*, 314, 376–388.

Rostami, M., Zeitlin, V. and Spiga, A. (2017) On the dynamical nature of Saturn's North Polar hexagon. *Icarus*, 297, 59–70.

Roundy, P.E. (2008) Analysis of convectively coupled Kelvin waves in the Indian ocean MJO. *Journal of the Atmospheric Sciences*, 65(4), 1342–1359.

Rui, H. and Wang, B. (1990) Development characteristics and dynamic structure of tropical intraseasonal convection anomalies. *Journal of the Atmospheric Sciences*, 47(3), 357–379.

Ruppert, J.H. and Johnson, R.H. (2015) Diurnally modulated cumulus moistening in the preonset stage of the Madden-Julian oscillation during DYNAMO. *Journal of the Atmospheric Sciences*, 72(4), 1622–1647.

Salby, M.L. (1989) Deep circulations under simple classes of stratification. *Tellus*, 41(1), 48–65.

Sánchez-Linares, C., Morales de Luna, T. and Castro Díaz, M. (2016) A HLLC scheme for Ripa model. *Applied Mathematics and Computation*, 272, 369–384.

Schopf, P.S. and Cane, M.A. (1983) On equatorial dynamics, mixed layer physics and sea surface temperature. *Journal of Physical Oceanography*, 13(6), 917–935.

Seo, K.-H. and Kumar, A. (2008) The onset and life span of the Madden-Julian oscillation. *Theoretical and Applied Climatology*, 94(1), 13–24.

Seviour, W.J.M., Waugh, D.W. and Scott, R.K. (2017) The stability of Mars's annular polar vortex. *Journal of the Atmospheric Sciences*, 74(5), 1533–1547.

Sobel, A. and Kim, D. (2012) The MJO–Kelvin wave transition. *Geophysical Research Letters*, 39, L20808.

Sperber, K. (2003) Propagation and the vertical structure of the Madden-Julian oscillation. *Monthly Weather Review*, 131, 3018–3037.

Straub, K.H. (2013) MJO initiation in the real-time multivariate MJO index. *Journal of Climate*, 26(4), 1130–1151.

Straub, K.H. and Kiladis, G.N. (2002) Observations of a convectively coupled Kelvin wave in the eastern Pacific ITCZ. *Journal of the Atmospheric Sciences*, 59(1), 30–53.

Straub, K.H. and Kiladis, G.N. (2003) Interactions between the boreal summer intraseasonal oscillation and higher-frequency tropical wave activity. *Monthly Weather Review*, 131(5), 945–960.

Trubbia, J. (1984) Modons in spherical geometry. *Geophysical and Astrophysical Fluid Dynamics*, 30, 131–168.

Vasil, G.M., Lecoanet, D., Burns, K.J., Oishi, J.S. and Brown, B.P. (2019) Tensor calculus in spherical coordinates using Jacobi polynomials. Part-I: mathematical analysis and derivations. *Journal of Computational Physics*, 3, 100013.

Verkley, W. (1984) The construction of barotropic modons on the sphere. *Journal of the Atmospheric Sciences*, 41, 2492–2504.

Vialard, J., Foltz, G.R., McPhaden, M.J., Duvel, J.P. and de Boyer Montgut, C. (2008) Strong Indian Ocean sea surface temperature signals associated with the Madden-Julian oscillation in late 2007 and early 2008. *Geophysical Research Letters*, 35(19), L19608. <https://doi.org/10.1029/10.1029/2008GL035238>

Vitart, F. and Molteni, F. (2010) Simulation of the Madden-Julian oscillation and its teleconnections in the ECMWF forecast system. *Quarterly Journal of the Royal Meteorological Society*, 136(649), 842–855.

Wang, B., Liu, F. and Chen, G. (2016) A trio-interaction theory for Madden-Julian oscillation. *Geoscience Letters*, 3(1), 34.

Wang, D., Yano, J.-I. and Lin, Y. (2019) Madden-Julian oscillations seen in the upper-troposphere vorticity field: interactions with Rossby wave trains. *Journal of the Atmospheric Sciences*, 76(6), 1785–1807.

Warneford, E.S. and Dellar, P.J. (2013) The quasi-geostrophic theory of the thermal shallow water equations. *Journal of Fluid Mechanics*, 723, 374–403.

Weickmann, K.M., Kiladis, G.N. and Sardeshmukh, P.D. (1997) The dynamics of intraseasonal atmospheric angular momentum oscillations. *Journal of the Atmospheric Sciences*, 54(11), 1445–1461.

Weickmann, K.M., Lussky, G.R. and Kutzbach, J.E. (1985) Intraseasonal (30–60 day) fluctuations of outgoing longwave radiation and 250 mb streamfunction during northern Winter. *Monthly Weather Review*, 113(6), 941–961.

Wheeler, M. and Kiladis, G.N. (1999) Convectively coupled equatorial waves: analysis of clouds and temperature in the wavenumber-frequency domain. *Journal of the Atmospheric Sciences*, 56(3), 374–399.

Wheeler, M.C. and Hendon, H.H. (2004) An all-season real-time multivariate MJO index: development of an index for

monitoring and prediction. *Monthly Weather Review*, 132(8), 1917–1932.

Xu, W. and Rutledge, S.A. (2015) Morphology, intensity, and rainfall production of MJO convection: observations from DYNAMO Shipborne Radar and TRMM. *Journal of the Atmospheric Sciences*, 72(2), 623–640.

Yano, J.-I., McWilliams, J.C., Moncrieff, M.W. and Emanuel, K.A. (1995) Hierarchical tropical cloud systems in an analog shallow-water model. *Journal of the Atmospheric Sciences*, 52(10), 1723–1742.

Yano, J.-I. and Tribbia, J. (2017) Tropical atmospheric Madden–Julian oscillation: a strongly nonlinear free solitary Rossby wave? *Journal of the Atmospheric Sciences*, 74, 3473–3489.

Yasunaga, K. and Mapes, B. (2012) Differences between more divergent and more rotational types of convectively coupled equatorial waves. Part II: composite analysis based on space-time filtering. *Journal of the Atmospheric Sciences*, 69(1), 17–34.

Zeitlin, V. (2018) *Geophysical Fluid Dynamics: Understanding (Almost) Everything with Rotating Shallow Water Models*. Oxford: Oxford University Press.

Zerroukat, M. and Allen, T. (2015) A moist Boussinesq shallow water equations set for testing atmospheric models. *Journal of Computational Physics*, 290, 55–72.

Zhang, C. (2005) Madden–Julian oscillation. *Reviews of Geophysics*, 43(2), 2004RG000158.

Zhang, C., Adames, A.F., Khouider, B., Wang, B. and Yang, D. (2020) Four theories of the Madden–Julian oscillation. *Reviews of Geophysics*, 58(3), e2019RG000685.

Zhang, C. and Ling, J. (2012) Potential vorticity of the Madden–Julian oscillation. *Journal of the Atmospheric Sciences*, 69(1), 65–78.

Zhao, B., Zeitlin, V. and Fedorov, A.V. (2021) Equatorial modons in dry and moist-convective shallow-water systems on a rotating sphere. *Journal of Fluid Mechanics*, 916, A8.

Zhu, L. and Li, T. (2017) A special MJO event with a double Kelvin wave structure. *Journal of Meteorological Research*, 31(2), 295–308.

How to cite this article: Rostami, M., Zhao, B. & Petri, S. (2022) On the genesis and dynamics of Madden–Julian oscillation-like structure formed by equatorial adjustment of localized heating. *Quarterly Journal of the Royal Meteorological Society*, 1–26. Available from: <https://doi.org/10.1002/qj.4388>

APPENDIX A. SUMMARY OF ANALYTIC SOLUTION OF ASYMPTOTIC MODON STRUCTURE

Following Rostami and Zeitlin (2019a), let us recall that the equation for the streamfunction of the equatorial

modon is derived from RSW equations in the equatorial β -plane with no dissipation:

$$\begin{cases} \partial_t \mathbf{v} + \mathbf{v} \cdot \nabla \mathbf{v} + \beta y \hat{\mathbf{k}} \wedge \mathbf{v} + g \nabla h = 0, \\ \partial_t h + \nabla \cdot (\mathbf{v} h) = 0, \end{cases} \quad (A1)$$

where $\nabla = (\partial_x, \partial_y)$, $\mathbf{v} = (u, v)$, u and v are zonal and meridional components of the velocity, h is geopotential height, β is the meridional gradient of the Coriolis parameter, and $\hat{\mathbf{k}}$ is a unit vertical vector. A small pressure perturbation ($\lambda \rightarrow 0$) can be included in the equations using parameter $\lambda: h = H(1 + \lambda\eta)$, where H is unperturbed geopotential height. Spatial, velocity and time-scales are $(x, y) \sim L$, $(u, v) \sim V$, $t \sim L/V$. Under the hypothesis that the characteristic velocity is much smaller than the phase velocity of the barotropic Kelvin waves, $c = \sqrt{gH}$, $V \ll \sqrt{gH}$, and $gH\lambda/V^2 = \mathcal{O}(1)$, hence, the nondimensional equations take the form

$$\partial_t \mathbf{v} + \mathbf{v} \cdot \nabla \mathbf{v} + \bar{\beta} y \hat{\mathbf{k}} \wedge \mathbf{v} + \nabla \eta = 0, \quad (A2)$$

$$\lambda(\partial_t \eta + \mathbf{v} \cdot \nabla \eta) + (1 + \lambda\eta) \nabla \cdot \mathbf{v} = 0, \quad (A3)$$

where $\bar{\beta} = \beta L^2/V$, and $\mathbf{v} = \mathbf{v}_0 + \lambda \mathbf{v}_1 + \dots$. In the leading order in λ , Equation A3 gives $\nabla \cdot \mathbf{v}_0 = 0$, the motion is non-divergent, and $u_0 = -\partial_y \psi$, $v_0 = \partial_x \psi$. The streamfunction can be extracted by cross-differentiation of the zonal and meridional momentum equations:

$$\nabla^2 \psi_t + \mathcal{J}(\psi, \nabla^2 \psi) + \bar{\beta} \psi_x = 0, \quad (A4)$$

where \mathcal{J} is Jacobian. The modon solutions are obtained under the hypothesis of steady motion with constant zonal velocity U , by assuming a linear relationship between the absolute vorticity and streamfunction in the comoving frame, which gives inhomogeneous Helmholtz equation. It is solved by separation of variables in polar coordinates in terms of Bessel functions, first in the outer domain under the decay condition, and then in the inner domain, and matching the inner and outer solutions across a circle of given radius a in the plane. The solution is in the form:

$$\begin{cases} \psi_{\text{ext}} = -\frac{Ua}{K_1(pa)} K_1(pr) \sin \theta, & r > a, \\ \psi_{\text{int}} = \left[\frac{Up^2}{\nu^2 J_1(\nu a)} J_1(\nu r) - \frac{r}{\nu^2} (1 + U + UV^2) \right] \sin \theta, & r < a, \end{cases} \quad (A5)$$

where J_1 and K_1 are ordinary and modified Bessel functions of order one, respectively, p is real, and $p^2 = \bar{\beta}/U$, so $U > 0$, meaning that the motion is *eastward*. For each pair (a, p) there exists a series of eigenvalues ν arising from matching conditions, of which the lowest corresponds to a

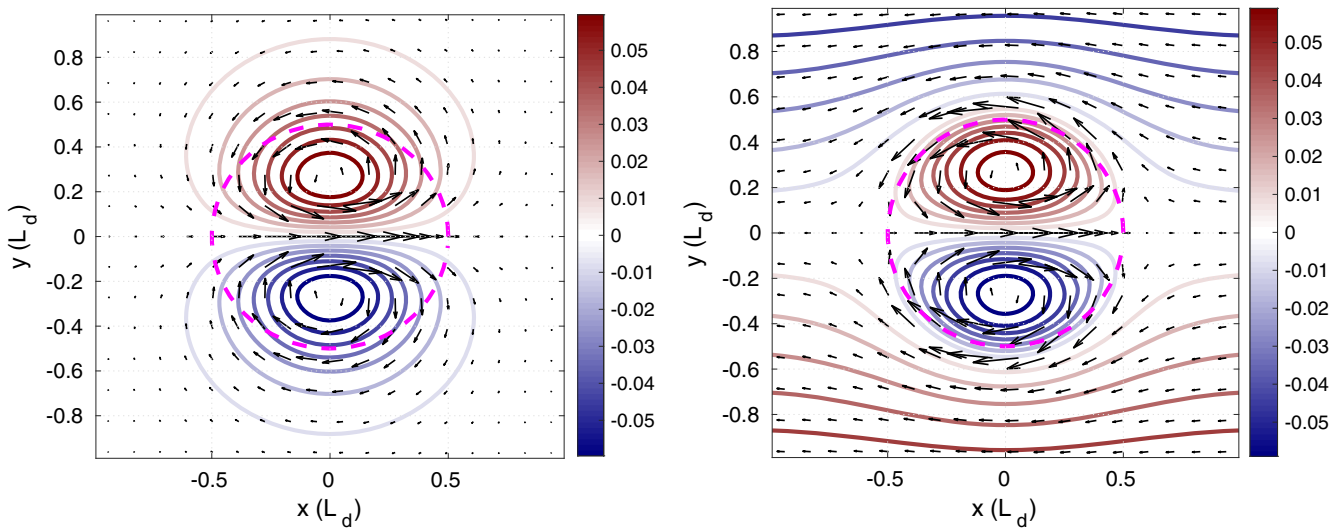


FIGURE A1 Streamlines and velocity field of an asymptotic modon in stationary (left panel) and comoving (right panel) frames with $U = 0.1$. Dashed circle: separatrix of radius $a = 0.5$ [Colour figure can be viewed at wileyonlinelibrary.com]

dipole, to be called the asymptotic modon. The next eigenvalue gives a quadrupolar solution called the “shielded modon,” and so on. The higher eigenvalues correspond to multipolar vortices with significant velocity shears in the

core, which are more sensitive to dissipation. Centering the solution in the equatorial β -plane leads to a cyclonic pair. The streamlines of the asymptotic modon according to Equations A5 are presented in Figure A1.